The Molecular Cloud Life Cycle. I. Constraining H₂ Formation and Dissociation Rates with Observations

Shmuel Bialy[1] , Blakesley Burkhart[2,3] , Daniel Seifried[4,5] , Amiel Sternberg[3,6], Benjamin Godard[7,8], Mark R. Krumholz[9] ,
Stefanie Walch[4,5] , Erika Hamden[10] , Thomas J. Haworth[11] , Neal J. Turner[12] , Min-Young Lee[13] , and Shuo Kong[10]

[1] Physics Department, Technion—Israel Institute of Technology, Haifa 32000, Israel; sbialy@technion.ac.il
[2] Department of Physics and Astronomy, Rutgers University, 136 Frelinghuysen Rd, Piscataway, NJ 08854, USA
[3] Center for Computational Astrophysics, Flatiron Institute, 162 Fifth Avenue, New York, NY 10010, USA
[4] I. Physics Institute, University of Cologne, Zülpicher Str. 77, 50937 Cologne, Germany
[5] Center for Data and Simulation Science, 50937 Cologne, Germany[14]
[6] Tel Aviv University, P.O. Box 39040, Tel Aviv 6997801, Israel
[7] Observatoire de Paris, Universite PSL, Sorbonne Universite, LERMA, 75014 Paris, France
[8] Laboratoire de Physique de l'Ecole Normale Superieure, ENS, Universite PSL, CNRS, Sorbonne Universite, Universite de Paris, F-75005 Paris, France
[9] Research School of Astronomy and Astrophysics, Australian National University, Canberra ACT 2600, Australia
[10] Steward Observatory, University of Arizona, Tucson, AZ 85719, USA
[11] Astronomy Unit, School of Physics and Astronomy, Queen Mary University of London, London, E1 4NS, UK
[12] Jet Propulsion Laboratory, California Institute of Technology, Pasadena, CA 91109, USA
[13] Korea Astronomy and Space Science Institute, 776 Daedeok-daero, Daejeon 34055, Republic of Korea
Received 2024 August 10; revised 2025 February 3; accepted 2025 February 3; published 2025 March 12

Abstract

Molecular clouds (MCs) are the birthplaces of new stars in galaxies. A key component of MCs are photodissociation regions (PDRs), where far-ultraviolet radiation plays a crucial role in determining the gas's physical and chemical state. Traditional PDR models assume a chemical steady state (CSS), where the rates of H₂ formation and photodissociation are balanced. However, real MCs are dynamic and can be out of CSS. In this study, we demonstrate that combining H₂ emission lines observed in the far-ultraviolet or infrared with column density observations can be used to derive the rates of H₂ formation and photodissociation. We derive analytical formulae that relate these rates to observable quantities, which we validate using synthetic H₂ line emission maps derived from the SILCC-Zoom hydrodynamical simulation. Our method estimates integrated H₂ formation and dissociation rates with an accuracy ≈30% (on top of the uncertainties in the observed H₂ emission maps and column densities). Our simulations, valid for column densities $N \leqslant 2 \times 10^{22}\,\mathrm{cm}^{-2}$, cover a wide dynamic range of H₂ formation and photodissociation rates, showing significant deviations from CSS, with 74% of the MC's mass deviating from CSS by a factor greater than 2. Our analytical formulae can effectively distinguish between regions in and out of CSS. When applied to actual H₂ line observations, our method can assess the chemical states of MCs, providing insights into their evolutionary stages and lifetimes. A NASA Small Explorer mission concept, Eos, will be proposed in 2025 and is specifically designed to conduct the types of observations outlined in this study.

Unified Astronomy Thesaurus concepts: Interstellar medium (847); Molecular clouds (1072); Ultraviolet spectroscopy (2284); Molecular gas (1073); Astrochemistry (75); Star formation (1569); Astrosphere interstellar medium interactions (106); Diffuse interstellar clouds (380)

1. Introduction

Molecular hydrogen (H₂), the most abundant molecule in the Universe, plays a crucial role in the life cycles of baryons throughout cosmic history (D. Galli & F. Palla 1998; C. F. McKee & E. C. Ostriker 2007; L. J. Tacconi et al. 2020). It acts as a vital cooling agent in the early Universe (Z. Haiman et al. 1996; K. Omukai 2000; R. Barkana & A. Loeb 2001; V. Bromm et al. 2001; S. Bialy & A. Sternberg 2019), triggers rich chemistry in the interstellar medium (ISM; E. Herbst & W. Klemperer 1973; A. G. G. M. Tielens 2013; E. F. van Dishoeck et al. 2013; S. Bialy & A. Sternberg 2015), and correlates with the star formation rate in present-day galaxies (F. Bigiel et al. 2008; A. K. Leroy et al. 2008; A. Schruba et al. 2011).

H₂ is predominantly found in molecular clouds (MCs) and is excited by far-ultraviolet (FUV) radiation within the Lyman–Werner (LW) band ($h\nu$ = 11.2–13.6 eV). LW photons excite the electronic $B^1\Sigma_u^+$ and $C^1\Pi_u$ states of H₂. These excited states can then radiatively decay through two pathways: (a) to the rovibrational continuum, leading to H₂ dissociation and the emission of FUV continuum radiation; or (b) to a bound (rovibrationally excited) level in the ground electronic state ($X^1\Sigma_g^+$), accompanied by FUV line emission (G. B. Field et al. 1966; T. P. Stecher & D. A. Williams 1967; A. Dalgarno et al. 1970; A. Sternberg 1989, hereafter S89). The rovibrationally excited H₂ molecules continue to cascade down the rovibrational ladder, emitting infrared (IR) lines (J. H. Black & E. F. van Dishoeck 1987; A. Sternberg 1988; M. L. Luhman et al. 1994; O. Goldshmidt & A. Sternberg 1995; B. T. Draine & F. Bertoldi 1996; D. A. Neufeld & M. Spaans 1996; H. A. N. Le et al. 2017; K. F. Kaplan et al. 2021).

In this study, we focus on photodissociation regions (PDRs), where radiative processes dominate molecular excitation and dissociation (A. G. G. M. Tielens & D. Hollenbach 1985; D. J. Hollenbach & A. G. G. M. Tielens 1999;

F. Le Petit et al. 2006; M. Röllig et al. 2007; T. G. Bisbas et al. 2021; M. Röllig & V. Ossenkopf-Okada 2022; M. W. Pound & M. G. Wolfire 2023). This includes gas in the vicinity of massive stars (e.g., the Orion nebula) and MCs embedded in the ambient interstellar radiation field, as long as the dust visual extinction is not too large. In contrast, in cloud cores, LW radiation is strongly attenuated due to H_2 self-shielding and dust absorption. In these well-shielded regions, H_2 excitation and dissociation are driven by deep-penetrating cosmic rays (CRs) or X-rays (P. R. Maloney et al. 1996; A. Dalgarno 2006; S. Bialy 2020; M. G. Wolfire et al. 2022). However, even for MCs exposed only to the ambient interstellar radiation field, photoprocesses dominate H_2 dissociation, excitation, and line emission up to gas column densities of $N \approx 10^{22}\,\mathrm{cm}^{-2}$ (M. Padovani et al. 2024; A. Sternberg et al. 2024; see also Section 5.2 of this paper and Appendix B).

Traditional PDR models assume that the total formation and destruction rates of H_2 (and other molecules) balance each other, i.e., that the system is in a chemical steady state (CSS). This allows the efficient characterization of MCs, since the abundance and emission spectra of H_2 are time-independent and depend only on physical conditions, such as the FUV radiation field intensity, gas density, and gas metallicity. For example, the CSS assumption allows the derivation of useful analytic formulae describing: (a) the atomic-to-molecular transition point (S. Bialy & A. Sternberg 2016); (b) the total H I column density (M. R. Krumholz et al. 2008, 2009; A. Sternberg et al. 2014; S. Bialy et al. 2017); and (c) the total intensity of the H_2 line emission (S89). This analytic framework has been utilized in the analysis of observations in various Galactic and extragalactic PDRs (e.g., S. Bialy et al. 2015; A. Ranjan et al. 2018; A. Schruba et al. 2018; P. Noterdaeme et al. 2019; J. Syed et al. 2022).

However, in practice, the assumption of CSS may be problematic. MCs are dynamic entities. They form in regions of converging flows (e.g., in gas that is infalling onto galactic spiral arms, collisions of expanding supernova shells, etc.), where gas may be compressed to high densities (H. Koyama & S.-I. Inutsuka 2000; L. Hartmann et al. 2002; E. Ntormousi et al. 2011; J. R. Dawson 2013; S. Bialy et al. 2021). Once gravitational collapse is initiated, newly formed stars begin to disperse the gas through various stellar feedback processes: ionizing radiation, stellar winds, jets, and supernova explosions (C. F. McKee & J. P. Ostriker 1977; C. A. Faucher-Giguère et al. 2013; P. F. Hopkins et al. 2020; M. E. Orr et al. 2022; E. C. Ostriker & C.-G. Kim 2022; M. Chevance et al. 2023). These dynamical processes can occur on short timescales compared to the time required for the gas to achieve CSS, and thus MCs may be out of CSS (S. C. O. Glover & M.-M. Mac Low 2007; M. R. Krumholz 2012; A. J. Richings et al. 2014; C.-Y. Hu et al. 2016; V. Valdivia et al. 2016; D. Seifried et al. 2017, 2022).

This raises an important question: can we determine from observations whether a given MC is in or out of CSS?

In this paper, we illustrate how combining the total intensity in the H_2 line emission with the total gas and H I column densities along the line of sight (LOS) allows us to obtain reliable estimates for the column-integrated rates of H_2 photodissociation and formation. This enables us to assess whether a CSS is maintained.

The question of whether an MC is in or out of CSS has important implications for the lifetimes and evolutions of MCs.

If the gas in an MC is found to be far from CSS, it implies that the MC has either been recently replenished with "fresh" gas or has lost gas via evaporation, over a timescale that is short compared to the chemical time (i.e., Equation (5) below; see also S. M. R. Jeffreson et al. 2024). In a second paper in this series (B. Burkhart et al. 2024), we explore in more detail the time evolutions of MCs, the evolutions of the H_2 formation and photodissociation rates in MCs, and their relationship to the star formation rate.

The structure of this paper is as follows. In Section 2, we provide the fundamental theoretical framework. We derive the key analytical equations—namely, Equations (9) and (12)—that elucidate how an observer can employ H_2 line emission intensities and column density maps to calculate integrated H_2 formation and dissociation rates along the LOS. In Section 3, we present the magnetohydrodynamical simulations and the numerical procedure for producing H_2 line intensity maps. We use these maps to test our analytic theory. In Section 4, we present our results, relating the state of the gas in the simulation and the H_2 formation and dissociation rates in various cloud regions to the observables. We follow up with a discussion and conclusions in Sections 5 and 6.

2. Theoretical Model

2.1. H_2 Formation and Dissociation

For typical ISM conditions, H_2 formation is dominated by dust catalysis (V. Wakelam et al. 2017). The destruction of H_2 is dominated by photodissociation. The net change in the number of H_2 molecules per unit time and volume is

$$\frac{dn(H_2)}{dt} = j_F - j_D, \tag{1}$$

where

$$j_F \equiv n(H)nR, \quad j_D \equiv n(H_2)D \tag{2}$$

are the volumetric H_2 formation and dissociation rates ($\mathrm{cm}^{-3}\,\mathrm{s}^{-1}$). Here, R ($\mathrm{cm}^3\,\mathrm{s}^{-1}$) is the H_2 formation-rate coefficient; D (s^{-1}) is the local photodissociation rate, which may be significantly attenuated due to H_2 self-shielding and dust absorption (see below); $n(H)$ and $n(H_2)$ are the H and H_2 number densities, respectively; and n is the total hydrogen nucleon density (in cm^{-3}). In Equation (2) and throughout our analytic model, we consider only H_2 photodissociation and neglect additional H_2 destruction via CRs. This assumption is justified in Section 5.2 and in Appendix B.

In this work, we use the "SImulating the Life-Cycle of molecular Clouds" (SILCC)-Zoom (D. Seifried et al. 2017) simulation suite to produce synthetic maps of H_2 line emission (as described below). In line with the SILCC simulation suite, we adopt an H_2 formation-rate coefficient

$$R = 3 \times 10^{-17} T_2^{1/2} S f_a Z_d' \, \mathrm{cm}^3\,\mathrm{s}^{-1}, \tag{3}$$

where $S = [1 + 0.4(T_2 + T_{d,2})^{0.5} + 0.2T_2 + 0.08T_2^2]^{-1}$ is the sticking coefficient; $f_a = [1 + 10^4 e^{-600\mathrm{K}/T_d}]^{-1}$ is the fraction of H atoms that enter the potential wells on the dust grain before evaporating and thus ultimately combining to form H_2 molecules (D. Hollenbach & C. F. McKee 1979); Z_d' is the dust-to-gas ratio relative to the solar neighborhood ISM; T and T_d are the gas and dust temperatures, respectively; and

$T_2 \equiv T/(10^2 \text{ K})$. The H_2 photodissociation rate is given by

$$D = \chi D_0 f_{H_2,\text{shield}} f_{\text{dust}}, \tag{4}$$

where $\chi = F_{\text{FUV}}/F_0$ is the flux of the incident FUV radiation field on the cloud relative to the typical solar neighborhood value, $F_0 = 2.7 \times 10^{-3} \text{ erg cm}^{-2}\text{ s}^{-1}$ (B. T. Draine 1978; S. Bialy 2020) and $D_0 = 5.8 \times 10^{-11} \text{ s}^{-1}$ is the free-space photodissociation rate in the absence of shielding (A. Sternberg et al. 2014). The functions $f_{H_2,\text{shield}}$ and f_{dust} account for LW attenuation by H_2 lines (self-shielding) and by dust absorption (see Section 3.1 and the discussion after Equations (A1)–(A2) for more details).

In CSS, $j_F = j_D$, and at any cloud position, the H_2-to-H ratio is then given by $n(H_2)/n(H) = Rn/D$. If $j_F \neq j_D$, the system is out of CSS: for $j_F > j_D$, there is net H_2 formation and the H_2 mass grows with time, whereas if $j_F < j_D$, the H_2 mass decreases with time.

For given values of D, R, and n, the timescale to reach CSS is

$$t_{\text{chem}} = \frac{1}{2nR + D}. \tag{5}$$

This follows from Equations (1)–(2) (see S. Bialy et al. 2017 for a discussion of this and other relevant timescales; see also O. Goldshmidt & A. Sternberg 1995; P. F. Goldsmith et al. 2007). Near cloud boundaries, where there is no LW attenuation, $D = \chi D_0 \gg 2Rn$. Under these conditions, the chemical time is very short: $t_{\text{chem}} = 1/(\chi D_0) = 550/\chi$ years. In deep cloud interiors, where radiation is significantly attenuated by dust and line absorption, $D \ll 2Rn$. In this regime, the chemical time equals the H_2 formation time:

$$t_{\text{chem}} \to t_{H_2,\text{form}} \equiv \frac{1}{2Rn} \approx 9\left(\frac{1}{Z'_d n_2}\right) \text{ Myr}, \tag{6}$$

where, for the numerical evaluation we used Equation (3) with typical cold neutral medium (CNM) conditions, $T = 100 \text{ K}$, $T_d \ll T$, and defined $n_2 \equiv n/(100 \text{ cm}^{-3})$. Thus, cloud envelopes, characterized by short chemical timescales, tend to be in CSS, while cloud interiors, which exhibit long chemical timescales, are prone to deviate from CSS.

Hereafter, we adopt typical solar neighborhood values for the FUV radiation field intensity and the dust-to-gas ratio, $Z'_d = 1$, $\chi = 1$.

2.2. Estimating H_2 Formation–Dissociation with Observations

In this subsection, we discuss how we can use emission-line observations to derive the H_2 formation and dissociation rates. As observations are probing integral quantities (integrated along the LOS) rather than volumetric quantities, we define the column-integrated H_2 formation and dissociation mass rates

$$\dot{\Sigma}_F^{(\text{true})} \equiv \bar{m} \int j_F ds = \bar{m} \int n(H) nR ds$$
$$\dot{\Sigma}_D^{(\text{true})} \equiv \bar{m} \int j_D ds = \bar{m} \int n(H_2) D ds, \tag{7}$$

where s is the coordinate along the LOS. The quantities $\dot{\Sigma}_F^{(\text{true})}$ and $\dot{\Sigma}_D^{(\text{true})}$ express the gas mass that is converted from atomic to molecular form and vice versa, per unit area and time ($M_\odot \text{ pc}^{-2}\text{ Myr}^{-1}$). We adopt a mean particle mass

$\bar{m} = 2m_H \times 1.4 = 4.7 \times 10^{-24}$ g, corresponding to the mass of an H_2 molecule, with the additional helium contribution assuming cosmic He abundance. We use the superscript "(true)" to stress that these are the true rates, as calculated by integrating the volumetric rates in our simulation. This is as opposed to the observationally estimated rates (defined below), which are derived from observable quantities such as H_2 line intensities and column densities.

2.2.1. The H_2 Photodissociation Rate

As discussed in Section 1, H_2 photodissociation occurs via a two-step process, in which first the electronic states of H_2 are photo-excited. The radiative decay to the rovibrational continuum of the ground electronic state leads to H_2 dissociation. The probability of dissociation per excitation is given by

$$p_{\text{diss}} \equiv D/P \approx 0.15, \tag{8}$$

where P is the total H_2 photo-excitation rate (of all H_2 electronic states; H. Abgrall et al. 1992; B. T. Draine & F. Bertoldi 1996). In the remaining 85% of cases, the H_2 decays to rovibrational bound states, producing FUV and subsequently IR line emission. In addition to line emission, H_2 electronic excitation also results in the emission of continuum FUV radiation (A. Dalgarno et al. 1970), which can also be observed and used to constrain the H_2 excitation and dissociation rates. In this paper, we focus on line emission, with our analytic and numerical analysis in Sections 2–4 concentrating on FUV lines. We then generalize to IR lines in Section 5.

Since the process of H_2 photo-excitation results in both line emission and H_2 dissociation, the H_2 dissociation rate is proportional to the total intensity of the H_2 emission lines. As we show in Appendix A (Equation (A6)), this relation is given by

$$\dot{\Sigma}_D^{(\text{obs})} = \frac{4\pi p_{\text{diss}} \bar{m}}{1 - p_{\text{diss}}} \mathcal{I}_{\text{tot}}\left(\frac{\tau_{\text{tot}}}{1 - e^{-\tau_{\text{tot}}}}\right)$$
$$= 0.30 \, \mathcal{I}_5\left(\frac{N_{21}}{1 - e^{-1.9N_{21}}}\right) M_\odot \text{ pc}^{-2} \text{ Myr}^{-1}, \tag{9}$$

where $\mathcal{I}_{\text{tot}}$ is the total photon intensity summed over all the FUV emission lines (photons $\text{cm}^{-2}\text{ s}^{-1}\text{ str}^{-1}$), and τ_{tot} is the dust opacity in the LW band. In Equation (9), we defined $\mathcal{I}_5 \equiv \mathcal{I}_{\text{tot}}/(10^5$ photons $\text{cm}^{-2}\text{ s}^{-1}\text{ sr}^{-1})$ and used $\tau_{\text{tot}} = \sigma N = 1.9 N_{21}$, where $\sigma = 1.9 \times 10^{-21}\text{ cm}^2$ (A. Sternberg et al. 2014) is the dust absorption cross section per hydrogen nucleus, N is the column density of hydrogen nuclei along the LOS, and $N_{21} \equiv N/(10^{21}\text{ cm}^{-2})$.

In Equation (9), we use the superscript "(obs)" to indicate that this expression approximates the true photodissociation rates, relying on integrated observable quantities, rather than the detailed 3D density structure, and radiation geometry information (see Appendix A). We note that in practice, observers typically measure only a subset of H_2 lines, rather than the total line emission $\mathcal{I}_{\text{tot}}$. However, theoretical methods exist to estimate $\mathcal{I}_{\text{tot}}$ from a subset of observed lines, using robust line ratios that are relatively insensitive to physical conditions (J. H. Black & E. F. van Dishoeck 1987; S89). The

detailed methodology for this conversion will be explored in future work.

The factor in parentheses expresses the absorption of the emitted H_2 lines by intervening dust. This factor connects smoothly the optically thin and thick regimes. In the optically thin limit ($\tau_{tot} \ll 1$), this factor approaches unity and $\dot{\Sigma}_D^{(obs)} \propto \mathcal{I}_{tot}$. In this limit, the H_2 emission lines directly trace the integrated H_2 photodissociation rate. On the other hand, in the optically thick limit ($\tau_{tot} > 1$), the factor $\tau_{tot}/(1 - e^{-\tau_{tot}}) \to \tau_{tot}$, and the ratio $\dot{\Sigma}_D^{(obs)}/\mathcal{I}_{tot}$ grows linearly with τ_{tot}. In this limit, $\mathcal{I}_{tot}$ traces only the outer part of the cloud, at an optical depth of ≈ 1. While the observed lines originate mainly from outer cloud envelopes, H_2 photodissociation can still occur deeper within clouds, as FUV radiation penetrates through lower-opacity regions in the patchy structure, not necessarily along the LOS.

For typical MCs in our Galactic neighborhood, $\tau_{tot} \approx 1$ ($N_{21} \approx 0.5$), $\mathcal{I}_5 \approx 0.3$–$0.6$,[15] and the integrated H_2 photodissociation rate is ≈ 0.1 $M_\odot\,pc^{-2}\,Myr^{-1}$.

2.2.2. The H_2 Formation Rate

Since H_2 formation involves H atoms that interact on dust grains, the integrated formation rate may be derived from observations of the H I column density (via the 21 cm emission line). To see this, we first define the effective mean Rn factor:

$$\langle Rn \rangle_{eff} \equiv \frac{\int (Rn) n(H) ds}{\int n(H) ds}. \tag{10}$$

Using this definition, we can rewrite Equation (7) as

$$\dot{\Sigma}_F^{(true)} = \bar{m} \langle Rn \rangle_{eff} N(H), \tag{11}$$

where $N(H)$ is the H column density.

First, let us gain intuition by considering a simple case of a uniform-density and uniform-temperature slab. In this case, Equation (10) simplifies to $\langle Rn \rangle_{eff} = Rn$. For typical CNM conditions, $n \approx 30$ cm^{-3} and $T = 100$ K (M. G. Wolfire et al. 2003; S. Bialy & A. Sternberg 2019). With Equation (3), we get $Rn = 5.4 \times 10^{-16}$ s^{-1}. For a CNM column density of 5×10^{20} cm^{-2}, we get an integrated H_2 formation rate of ≈ 0.2 $M_\odot\,pc^{-2}\,Myr^{-1}$.

In practice, the gas density and temperature vary inside the cloud, and the value of $\langle Rn \rangle_{eff}$ differs from one LOS to another. 3D dust maps offer insights into density structure (e.g., R. Leike et al. 2020; C. Zucker et al. 2021), but they lack the resolution to capture the critical H I–H_2 transition length. This transition, occurring over scales $\lesssim 1$ pc (S. Bialy et al. 2017), is crucial for studying the H–H2 balance and chemical states of clouds. Due to this resolution limitation, we must rely on readily observable LOS-integrated quantities to estimate $\langle Rn \rangle_{eff}$. From a theoretical point of view, $\langle Rn \rangle_{eff}$ is expected to correlate with the integrated gas column density N. This is because particles that are situated in large reservoirs of mass will typically have a large integrated column density along the LOS (i.e., large N), while, on the other hand, these particles are situated in deeper gravitational potential wells, leading to gas compression (i.e., higher n).

This correlation has been observed in various independent hydro simulations of the ISM (i.e., the A_V–n relation; T. G. Bisbas et al. 2019, 2021; C.-Y. Hu et al. 2021; B. A. L. Gaches et al. 2022). Using our SILCC-Zoom simulations, we find that $\langle Rn \rangle_{eff}$ is well described by the power-law relation $\langle Rn \rangle_{eff} = k_0 N_{21}^\alpha$, with $k_0 = 2.0 \times 10^{-16}$ s^{-1} and $\alpha = 1.3$. With this power-law relation, we get

$$
\begin{aligned}
\dot{\Sigma}_F^{(obs)} &= \bar{m} k_0 N_{21}^\alpha N(H) \\
&= 0.14 \quad f_H N_{21}^{1+\alpha} \ M_\odot\,pc^{-2}\,Myr^{-1},
\end{aligned} \tag{12}
$$

where $\alpha = 1.3$ and where we defined $f_H \equiv N(H)/N$.

Similar to the case of $\dot{\Sigma}_D^{(obs)}$, here, too, we use the superscript "(obs)" to emphasize that $\dot{\Sigma}_F^{(obs)}$ is derived based on observed quantities only and is an approximation to the true rate. In Section 4, we test the accuracy of these approximations using our hydro simulations.

2.2.3. The Formation-to-photodissociation-rate Ratio

Combining Equations (9) and (12), we obtain the formation-to-dissociation-rate ratio:

$$
\begin{aligned}
\left(\frac{\dot{\Sigma}_F}{\dot{\Sigma}_D} \right)^{(obs)} &= \frac{k_0 N_{21}^\alpha N(H)}{4\pi \mathcal{I}_{tot} \left(\frac{\tau_{tot}}{1 - e^{-\tau_{tot}}} \right)} \frac{1 - p_{diss}}{p_{diss}}, \\
&= 0.47 \quad N_{21}^\alpha f_H (1 - e^{-1.9 N_{21}}) \mathcal{I}_5^{-1}.
\end{aligned} \tag{13}
$$

If CSS holds, $\dot{\Sigma}_F/\dot{\Sigma}_D = 1$. If $\dot{\Sigma}_F/\dot{\Sigma}_D > 1$, then the gas along the LOS is not in CSS, and the H_2 column density increases with time at the expense of H I. If $\dot{\Sigma}_F/\dot{\Sigma}_D < 1$, the H_2 column density decreases with time and H I increases. Thus, given an observation of the gas H I and total column density and an H_2 emission spectrum, we can constrain the chemical state of the gas and whether it is in CSS or not.

3. Numerical Method

3.1. Hydro Simulations

We generate synthetic maps of the H_2 line emission, formation rate, and dissociation rate using the SILCC-Zoom simulations (D. Seifried et al. 2017). These are high-resolution zoom-in runs derived from the SILCC simulation suite (P. Girichidis et al. 2016; S. Walch et al. 2015). The SILCC simulation suite is a set of magnetohydrodynamical models of the chemical and thermal states of the ISM and the formation of stars in realistic galactic environments. The SILCC simulations have a stratified-box geometry. They include self-gravity as well as a background potential for the Galactic disk. Each simulation follows the thermal evolution of the gas and dust, including photoelectric heating by dust, CR ionization heating, and radiative cooling through various atoms, ions, and molecules. The chemistry of the ISM is modeled using an "on-the-fly" time-dependent network for hydrogen and carbon chemistry, tracking the evolution of the chemical abundances of free electrons, O, H^+, H, H_2, C^+, and CO. The simulation models H–H_2 chemistry, encompassing H2 formation on dust, photodissociation, photoionization, and CR ionization. It also accounts for the attenuation of nonionizing LW radiation through dust absorption (f_{dust}) and H_2 self-shielding ($f_{H_2,shield}$). These attenuation factors, as represented in Equation (4), are calculated using the TreeRay algorithm

---

[15] This follows from scaling the results of S89 to $\chi = 1$. S89 obtained a total H_2 line intensity of 1.1×10^{-4} erg $cm^{-2}\,s^{-1}\,sr^{-1}$ for his fiducial $\chi = 100$, $n = 10^3$ cm^{-3} model. As discussed in S89, these parameters correspond to the "weak-field" limit, in which $\mathcal{I}_{tot} \propto \chi$. Scaling the results of S89 to $\chi = 1$ and dividing by a mean photon energy $\langle h\nu \rangle = 11.2$ eV, we obtain $\mathcal{I}_5 = 0.6$.

Table 1
Simulation Properties and Chemical State Overview

Quantity	Value
Simulation side length	125 pc
Resolution	512^3
Simulation time (fiducial snapshot)	3 Myr
Mean density	3.3 cm^{-3}
Radiation field strength (χ)	1
Total gas mass	$2.2 \times 10^5 M_\odot$
Fraction of gas out of CSS	41% (by volume)
	74% (by mass)

Note. The table is divided into two sections. The top section summarizes the simulation setup, including key physical parameters. The bottom section provides an overview of the chemical state of the gas, with CSS defined as cells satisfying $0.5 < (j_F/j_D) < 2$. For summary statistics of additional time snapshots, see Table 2.

(R. Wünsch et al. 2018), which considers radiation propagating along multiple directions for each cell.

The SILCC-Zoom simulations enhance the base SILCC framework by implementing adaptive mesh refinement, where regions of impending MC formation are resolved down to 0.12 pc scales, compared to the base 4 pc resolution used for driving turbulence through supernova injection. The specific zoom-in run used herein is the "MC1-MHD" simulation, which contains an initial magnetic field with a strength of $3 \mu G$, described first in detail in D. Seifried et al. (2019, 2020).

In this paper, we evaluate the reliability of using H$_2$ emission lines in combination with gas column densities to trace H$_2$ formation and dissociation rates. Specifically, we investigate whether the method described in Section 2.2 can accurately identify regions that deviate from CSS. For our analysis, we focus on a snapshot taken at 3 Myr after initiating the zoom-in procedure. No star formation was considered in the simulations, allowing us to focus on the formation process of the cloud itself. At this point, the effects of non-CSS conditions are most pronounced. While this represents a simplified scenario compared to realistic star-forming clouds, it allows us to establish and validate our methodology in a controlled setting. The extension to more complex environments, including actively star-forming regions and the effects of supernova/stellar feedback, is explored in our companion paper (B. Burkhart et al. 2024). We note that our analysis is most applicable to clouds with column densities $N \lesssim 2 \times 10^{22}$ cm^{-2}, where CR ionization and excitation remains subdominant (see Section 5.2 and Appendix B).

For the analysis presented in this paper, we map the zoom-in region over an extent of $(125 \text{ pc})^3$ to a uniformly resolved grid with a resolution of 0.244 pc, i.e., 512^3 cells. The general properties of the extracted volume are given in Table 1. We consider additional time snapshots and quantify the robustness of our analysis in Appendix C.

3.2. Synthetic Observations

The SILCC-Zoom simulations output the atomic, molecular, and total H nuclei volume densities—$n(H)$, $n(H_2)$, and n, respectively; the gas and dust temperatures—T and T_d, respectively; and the LW radiation attenuation factors, $f_{H_2,\text{shield}}$ and f_{dust}, on a cell-by-cell basis. With these outputs, we derive the H$_2$ line emission map ($\mathcal{I}_{\text{tot}}$) as follows:

1. We consider the observer–cloud LOS extending along the x-axis direction.
2. For each cell at "sky" position y, z, and depth x in the simulation, the hydrogen nucleus column density from that cell to the observer is $N(x, y, z) = \int_0^x n(x', y, z)dx'$, and the corresponding optical depth is $\tau(x, y, z) = \sigma N(x, y, z)$.
3. For each cell in the simulation (x, y, z), we have the optical depth $\tau(x, y, z)$, the local photodissociation rate D (Equation (4) with $\chi = 1$), and the local excitation rate $P = D/p_{\text{diss}} \approx D/0.15$ (Equation (8)). Using these quantities, we calculate the 2D map of $\mathcal{I}_{\text{tot}}$ for all LOSs (y, z), using Equation (A2), where the integration is along x.
4. We repeat steps 1–3 for the other two LOS orientations, LOSs along the y- and z-axes.

At the conclusion of steps 1–4, we obtain maps of the H$_2$ emission-line intensity, $\mathcal{I}_{\text{tot}}$, for three LOS orientations. These maps are presented in Section 4.2. It is important to note that our synthetic observations are idealized, as they do not account for the limitations of observational instruments.

Utilizing Equation (9), we convert $\mathcal{I}_{\text{tot}}$ to $\dot{\Sigma}_D^{\text{(obs)}}$. In what follows (Sections 4.2–4.3), we compare these observationally derived rates, $\dot{\Sigma}_D^{\text{(obs)}}$, with the true rates, $\dot{\Sigma}_D^{\text{(true)}}$, as given by directly integrating the volumetric formation and dissociation rates in the simulation (Equation (7)). This comparison addresses how well the total H$_2$ line intensity traces the H$_2$ photodissociation rate. Similarly, we derive $\dot{\Sigma}_F^{\text{(obs)}}$ and compare it with the true formation rate given by the simulation $\dot{\Sigma}_F^{\text{(true)}}$. To obtain $\dot{\Sigma}_F^{\text{(obs)}}$, we utilize the H I column density, $N(H)$, and the total (H I+H$_2$) gas column density, N, obtained from the simulation data. We then use Equation (12) to derive $\dot{\Sigma}_F^{\text{(obs)}}$. As is the case for $\dot{\Sigma}_D^{\text{(obs)}}$, the formation rate $\dot{\Sigma}_F^{\text{(obs)}}$ is an approximation for the true rate, as it relies on an average relation (Equation (12)) that uses integrated quantities (which can be observed) as inputs, as opposed to the real, cell-by-cell volumetric formation rates.

Our analysis assumes the availability of reliable total-gas-column-density maps. In practice, deriving such maps from observations requires careful consideration of multiple tracers: H I 21 cm emission for atomic gas, CO lines with appropriate X_{CO} conversion factors (A. D. Bolatto et al. 2013), and dust continuum emission assuming dust-to-gas ratios and emissivity laws (Planck Collaboration et al. 2011). These conversions can introduce uncertainties of factors of 2–3 in the derived column densities. While these observational challenges are crucial for applying our method to real data, addressing them is beyond the scope of this paper. Instead, in this paper, we focus on the subsequent question: given maps of H I and total gas column density derived from observations, how well can we constrain H$_2$ formation and dissociation rates and assess whether the gas is in CSS?

In Sections 4.2–4.3, we compare $\dot{\Sigma}_F^{\text{(obs)}}$ with $\dot{\Sigma}_F^{\text{(true)}}$ by directly integrating the volumetric H$_2$ formation rate, cell by cell, along the LOS (Equation (7)).

4. Results

4.1. Volumetric Quantities

Before presenting the integrated H$_2$ formation/dissociation rates, we begin by exploring key volumetric quantities. This provides intuition regarding the conditions in the simulation box. In all figures, log denotes the logarithm base 10.
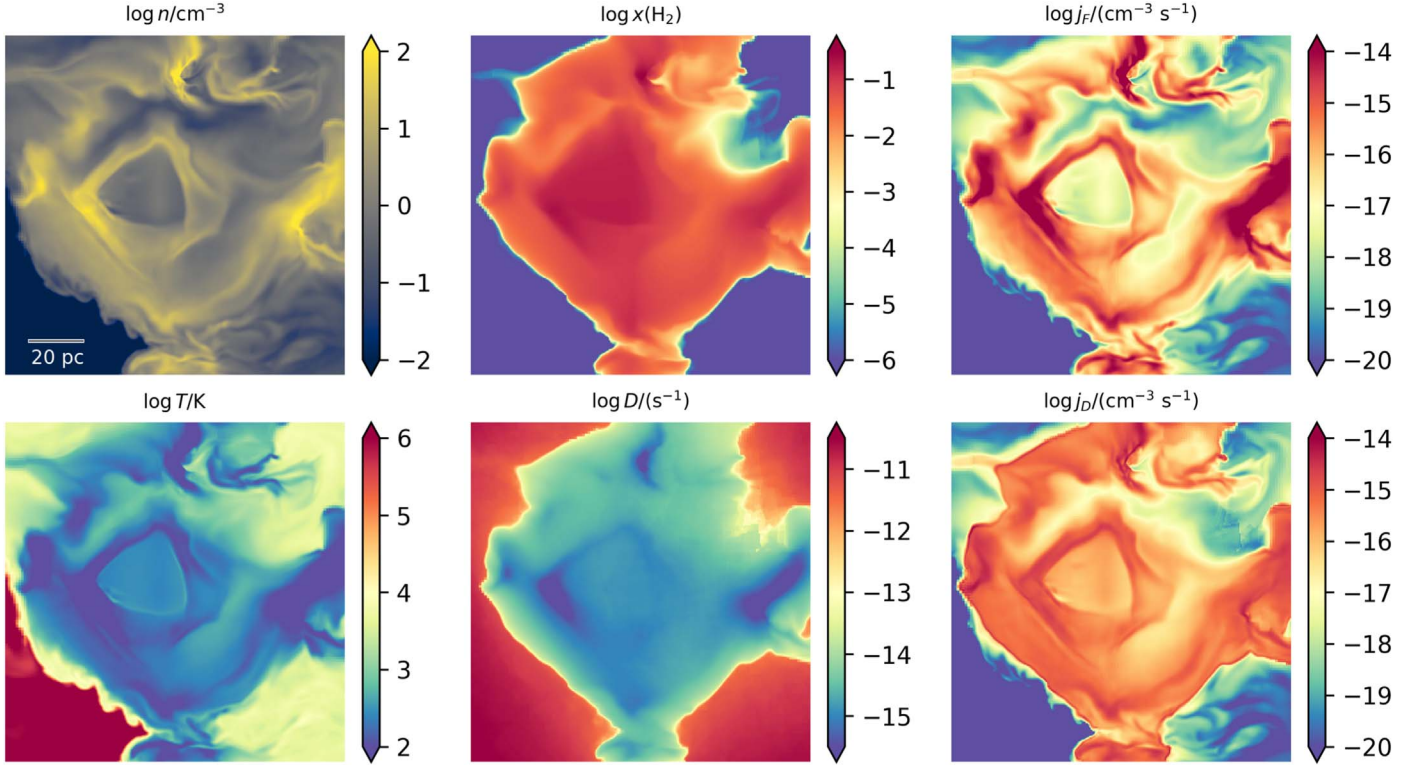
Figure 1. A 2D slice (xy plane) through the SILCC-Zoom simulation. The box size is 125 pc × 125 pc. The different panels show the gas density, the gas temperature, the H$_2$ abundance ($x(H_2) \equiv n(H_2)/n$), the H$_2$ photodissociation rate (Equation (4)), and the volumetric H$_2$ formation and photodissociation rates (Equation (2)). For an interactive figure, see sbialy.wixsite.com/astro/visuals.

Figure 1 illustrates the cloud's density structure and its chemical state. It shows a 2D slice parallel to the xy plane sliced at the middle of the z-axis. The six panels correspond to various fields: the gas density n, the gas temperature T, the H$_2$ abundance $x(H_2) \equiv n(H_2)/n$, the local H$_2$ (shielded) photodissociation rate D (Equation (4)), and the volumetric H$_2$ formation and photodissociation rates, j_F and j_D (Equation (2)). The gas is highly inhomogeneous, with density and temperature spanning large ranges. Due to the absorption of the FUV radiation, the cloud interior is mostly cold, with $T \lesssim 100$ K. This attenuation of the radiation intensity with cloud depth is also evident in the maps of $x(H_2)$ and D, where we see a sharp decrease in the photodissociation rate and a sharp increase in the H$_2$ abundance from the cloud edge to the cloud interior. The clumpy density structure of the cloud, as well as time-dependent chemical effects, result in inhomogeneous structures of j_F and j_D where often the two are not in balance.

In Figure 2, we present the probability density function (PDF) of j_F/j_D (Equation (2)), weighted by mass (left) and volume (right). The PDFs are composed of two components: a sharp peak at $\log j_F/j_D = 0$, which arises from gas cells that are in CSS, and a broad component spanning a large range of out-of-CSS gas.

To get insight onto these two populations, in Figure 3 we plot the joint distribution (mass-weighted) of j_F/j_D versus various volumetric quantities: (a) the gas number density, n; (b) the effective dust extinction, $A_{V,\mathrm{eff}}$;[16] (c) the gas temperature, T; (d) the H$_2$ abundance, $x(H_2)$; (e) the local H$_2$ photodissociation rate, D (Equation (4)); and (f) the timescale required to reach
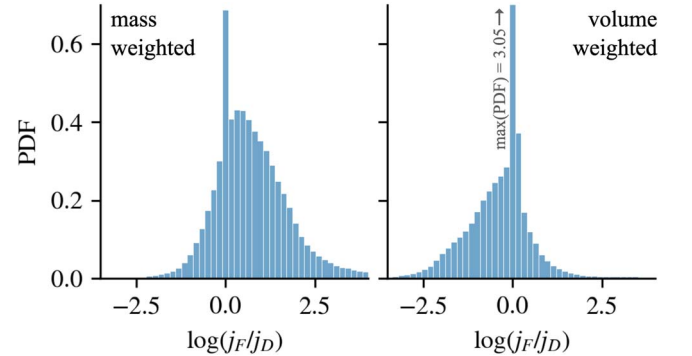

Figure 2. The 1D PDF of $\log j_F/j_D$, weighted by mass (left) and volume (right). Each PDF is composed of a population of cells that are in CSS (the peak is at $\log j_F/j_D = 0$) and a wide and prominent distribution of gas that is out of CSS (see also Table 1).

CSS, t_{chem} (Equation (5)). Looking at the 2D distributions in Figure 3, we see these two populations. In the upper panels, we see that the CSS population corresponds to gas that is relatively diffuse and warm, with $n \sim 0.1$–3 cm^{-3} and $T \approx 300$–6000 K, and that has low visual extinctions, $A_V,\mathrm{eff} \lesssim 0.25$. This gas is located closer to the cloud boundaries and is exposed to relatively strong FUV radiation. Indeed, from the D and x_{H2} PDFs, we see that the CSS gas experiences high dissociation rates $D \approx 10^{-12}$–10^{-10} s^{-1} (i.e., little attenuation) and is predominantly atomic with $x(H_2) \lesssim 10^{-5}$. The timescale to achieve CSS for such conditions is the H$_2$ photodissociation time and is very short, $t_{\mathrm{chem}} \simeq 1/D \sim (0.03$–3$) \times 10^4$ yr, thus the gas is in CSS.

The gas that is in CSS occupies a significant volume fraction, but it includes only a small fraction of the MC mass. Most of the

---

[16] $A_{V,\mathrm{eff}}$ is defined as a weighted mean of A_V from the cell to the cloud edge for different rays and is related to the dust shielding factor through $f_{\mathrm{dust}} = e^{-3.5A_{V,\mathrm{eff}}}$ (D. Seifried et al. 2020).
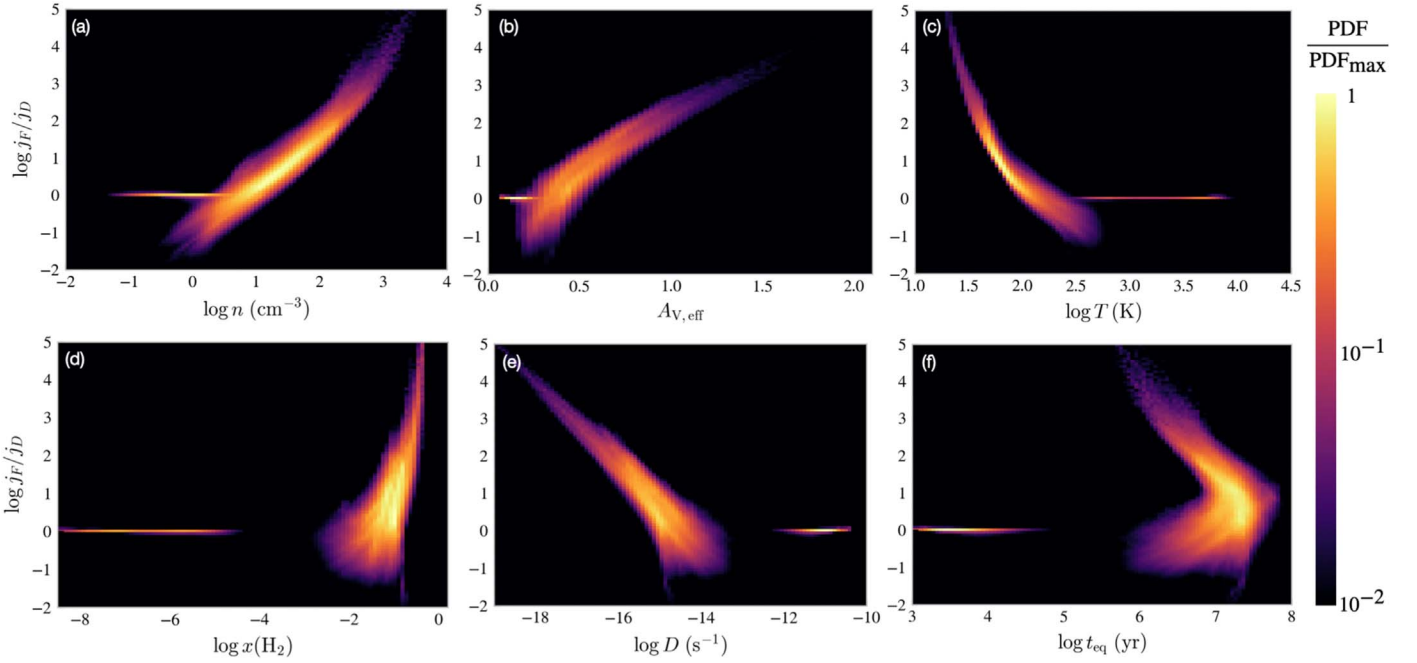
Figure 3. Mutual 2D mass-weighted PDFs of volumetric quantities in the simulation box. We show 2D PDFs of $\log j_F/j_D$ vs. (a) gas density; (b) effective dust extinction; (c) gas temperature; (d) H_2 fraction; (e) local (attenuated) photodissociation rate; and (f) chemical timescale (see the text for details). These PDFs reveal two distinct populations: (1) a warm, diffuse, and H_2-poor gas, located in low-shielded regions, which has achieved CSS (i.e., the narrow horizontal strips at $\log j_F/j_D = 0$); and (2) cold, dense H_2-rich, well-shielded gas, which is out of CSS and exhibits a wide j_F/j_D distribution.

mass is found in out-of-CSS gas (see also D. Seifried et al. 2022). This population shows up in Figure 3 as the wide distribution of pixels extending from $\log j_F/j_D \sim -2$ to ~ 4. This gas is typically denser and colder, $n \sim 1$–10^3 cm^{-3}, $T \approx 20$–300 K, and is located in inner-cloud regions with A_V, eff $= 0.25$–1.5. This gas is exposed to low FUV intensities ($D \lesssim 10^{-14}$ s^{-1}) and is H_2-rich ($x(H_2) \gtrsim 10^{-2}$). Under these conditions, the chemical timescale is long, $t_{\text{chem}} \simeq 1/(2Rn) \approx 1$–$100$ Myr, and the gas has not had sufficient time to reach CSS.

Qualitatively, defining CSS as regions where the H_2 formation and dissociation rates differ by less than a factor of 2 (i.e., $0.5 < (j_F/j_D) < 2$), we find that only 26% of the simulation mass is in CSS (see Table 1). The volume fraction of cells that are in CSS is 59%. The volume fraction is higher than the mass fraction because the CSS regions reside near cloud boundaries where the gas is typically more diffuse and thus occupies larger volumes.

Integrating j_F and j_D over the MC volume, we obtain a total H_2 formation rate $\dot{M}_F^{(\text{true})} = 8.6 \times 10^3$ $M_\odot$ Myr^{-1}, a dissociation rate $\dot{M}_D^{(\text{true})} = 1.1 \times 10^3$ $M_\odot$ Myr^{-1}, and a net H_2 formation $\dot{M}_{H_2}^{(\text{true})} = \dot{M}_F^{(\text{true})} - \dot{M}_D^{(\text{true})} = 7.5 \times 10^3$ $M_\odot$ Myr^{-1}. This net positive formation rate indicates that if the cloud were to maintain these gas conditions for a sufficiently long time ($t > t_{\text{chem}}$), a significant mass of H I would eventually convert to H_2. Consequently, the reduced HI fraction would cause j_F to decrease (see Equation (2)) until it finally equilibrates with j_D, at which point the gas reaches CSS. In Paper II of this series (B. Burkhart et al. 2024), we explore the evolution of H_2 formation and dissociation rates over the dynamical timescales of MCs.

4.2. 2D Maps

Figure 4 presents maps of the total H_2 line emission, $\mathcal{I}_{\text{tot}}$, for three LOS orientations, generated following the procedure described in Section 3.2. These maps simulate the observations

an astronomer might obtain by directing an FUV spectrograph toward an MC and aggregating all observed H_2 line intensities.

Figure 5 compares the 2D maps of the true H_2 photodissociation rate, $\dot{\Sigma}_D^{(\text{true})}$, and the observer-derived rate, $\dot{\Sigma}_D^{(\text{obs})}$. The true rate is calculated by integrating the volumetric photodissociation rate cell by cell in the simulation (Equation (7)), while the observer-derived rate is obtained from the H_2 line emission maps (Equation (9); see also Section 3.2). For the three LOS orientations, the observer-derived maps effectively recover the true H_2 dissociation maps over a large dynamic range of photodissociation rates, from $\dot{\Sigma}_D = 10^{-2}$ to $10 M_\odot$ pc^{-2} Myr^{-1}. As discussed in Section 2.2.1, the observationally derived rates and true rates are not identical, because an observer does not have access to the true value of the attenuation factor and must rely on integrated quantities (i.e., see Appendix A; Equation (A5) versus Equation (A3)).

Figure 6 shows the true and observationally derived H_2 formation-rate maps. Here, again, we observe that the overall structure of the observationally derived H_2 formation-rate map qualitatively agrees with the true formation-rate map, spanning from weakly H_2-forming regions with $\dot{\Sigma}_F = 0.01$ $M_\odot$ pc^{-2} Myr^{-1} to highly efficient H_2-forming regions with $\dot{\Sigma}_F = 10$ $M_\odot$ pc^{-2} Myr^{-1}.

Integrating $\dot{\Sigma}_D$ and $\dot{\Sigma}_F$ over the area, we obtain the total H_2 formation and dissociation mass rates. Using the observationally derived surface densities $\dot{\Sigma}_D^{(\text{obs})}$ and $\dot{\Sigma}_F^{(\text{obs})}$ (Equations (9) and 12), we obtain $\dot{M}_F^{(\text{obs})} = (9.3, 10.8, 7.3) \times 10^3 M_\odot$ Myr^{-1} and $\dot{M}_D^{(\text{obs})} = (1.4, 1.5, 1.1) \times 10^3 M_\odot$ Myr^{-1} for the x, y, and z LOS orientations, respectively. We compare these measurements with the true mass rates (independent of orientation): $\dot{M}_F^{(\text{true})} = 8.6 \times 10^3$ $M_\odot$ Myr^{-1} and $\dot{M}_D^{(\text{true})} = 1.1 \times 10^3$ $M_\odot$ Myr^{-1}. The true rates are obtained by integrating $\dot{\Sigma}_D^{(\text{true})}$
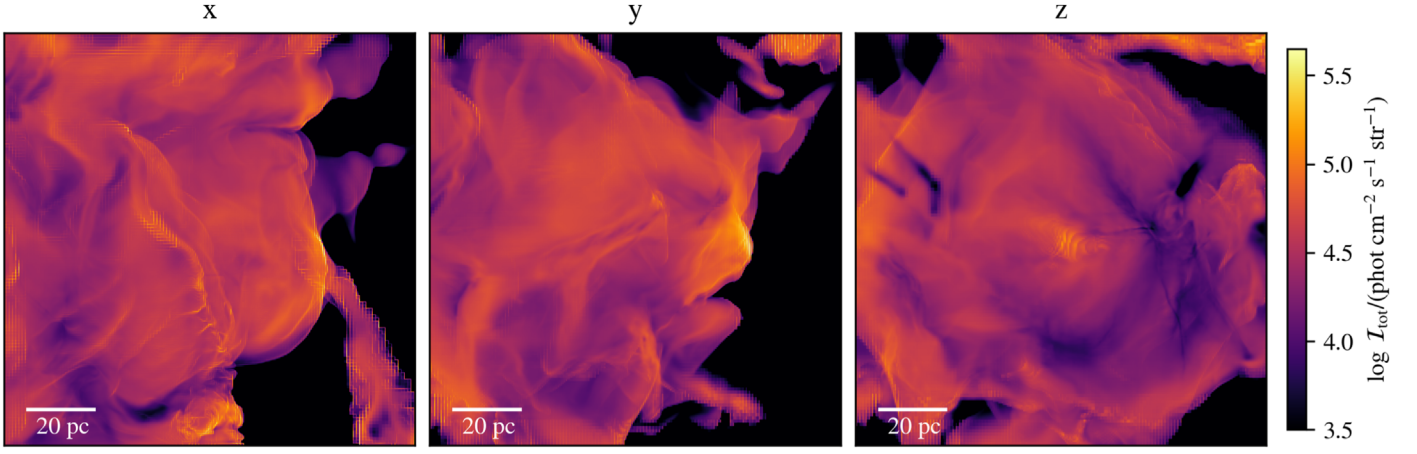
Figure 4. H_2 line emission maps. The panels show the H_2 emission-line intensity (summed over all emission lines) for three orientations of the observer's LOS (see Section 3.2 for details).
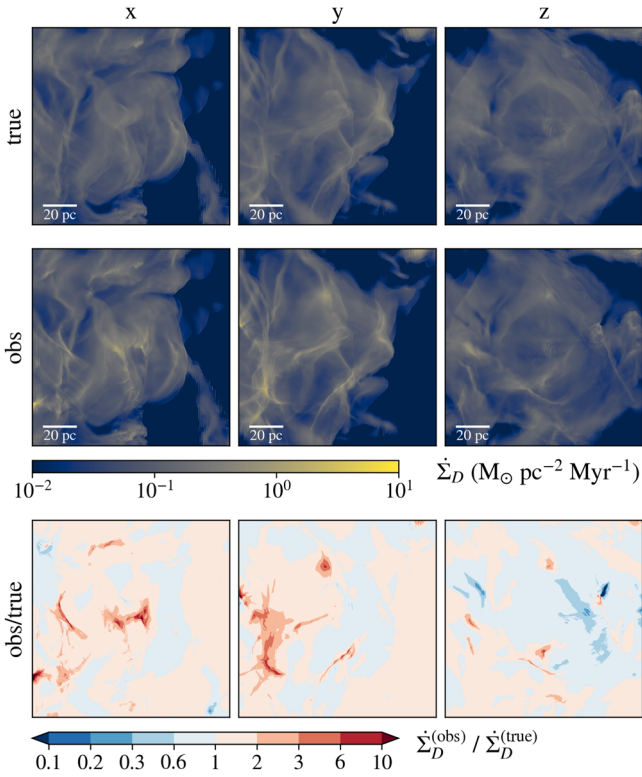

Figure 5. Integrated H_2 photodissociation-rate maps. Top: maps of the *true* photodissociation rate, $\dot{\Sigma}_D^{(\text{true})}$, as calculated by integrating the volumetric photodissociation rate (Equation (7)). Middle: the observationally derived rate, $\dot{\Sigma}_D^{(\text{obs})}$, as derived from the H_2 line emission map, $\mathcal{I}_{\text{tot}}$ (Equation (9); Section 3.2). Bottom: the ratio $\dot{\Sigma}_D^{(\text{obs})}/\dot{\Sigma}_D^{(\text{true})}$.

and $\dot{\Sigma}_F^{(\text{true})}$ (Equation (7)) or, equivalently, by volumetrically integrating j_F and j_D (Equation (2)).

To assess the robustness of these results, we extend this analysis to different simulation snapshots ($t = 2, 3, 4,$ and 5 Myr) in Appendix C, comparing the observationally derived rates with the true values. Across all realizations (four snapshots × three LOS orientations), the observationally derived rates agree with the true rates to within a mean relative difference of 27% for H_2 formation and 31% for H_2 dissociation (see Table 1 for detailed statistics).
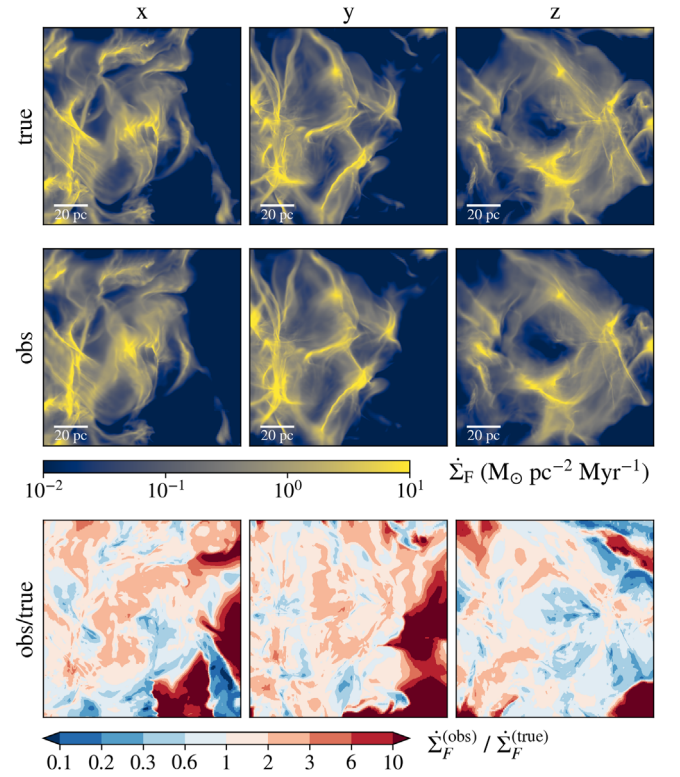
Figure 6. The same as Figure 5 but for the H_2 formation rate.

4.3. PDFs of $\dot{\Sigma}_D$ and $\dot{\Sigma}_F$

Figure 7 shows the mass-weighted PDFs of $\dot{\Sigma}_D$, $\dot{\Sigma}_F$, and $\dot{\Sigma}_F/\dot{\Sigma}_D$. For these PDFs, we stack the data for the three LOS orientations, x, y, and z. In each panel, the blue histograms correspond to the true rates and the red to the observationally derived rates. Qualitatively, the observational PDFs provide a good approximation to the true PDFs, recovering the general shape, average position, and PDF dispersion. Quantitatively, we find that there are (small) statistical differences. For example, the mass-weighted average and standard deviation of $\log \dot{\Sigma}_D$ are $(\mu, \sigma) = (-1.03, 0.40)$ for the "true" PDF and $(-0.94, 0.50)$ for the "observed" PDF. For $\log \dot{\Sigma}_F$, we find $(\mu, \sigma) = (-0.25, 0.87)$ for the "true" PDF and $(-0.20, 0.85)$ for the "observed" PDF.
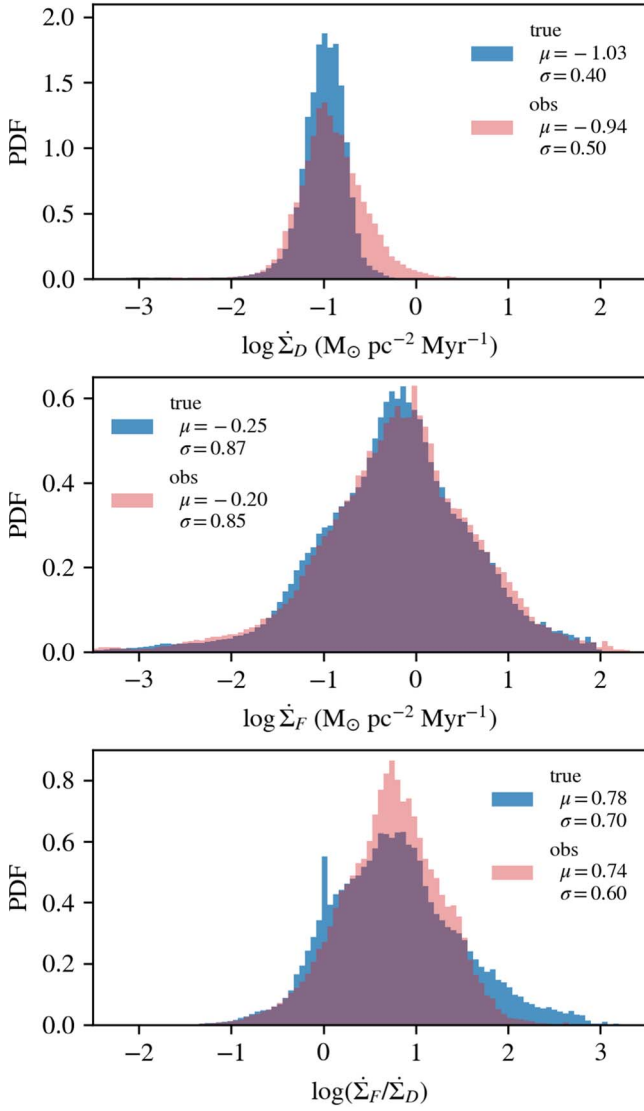
Figure 7. Mass-weighted-rate PDFs. The PDFs of the H$_2$ photodissociation rate, $\log \dot{\Sigma}_D$ (top); the H$_2$ formation rate, $\log \dot{\Sigma}_F$ (middle); and their ratio, $\log(\dot{\Sigma}_F/\dot{\Sigma}_D)$ (bottom). For these PDFs, we stack data for the three LOS orientations x, y, and z. Each panel compares the observationally-derived-rate (Equations (9) and (12)) and the true-rate (Equation (7)) PDFs . The means and standard deviations are indicated.
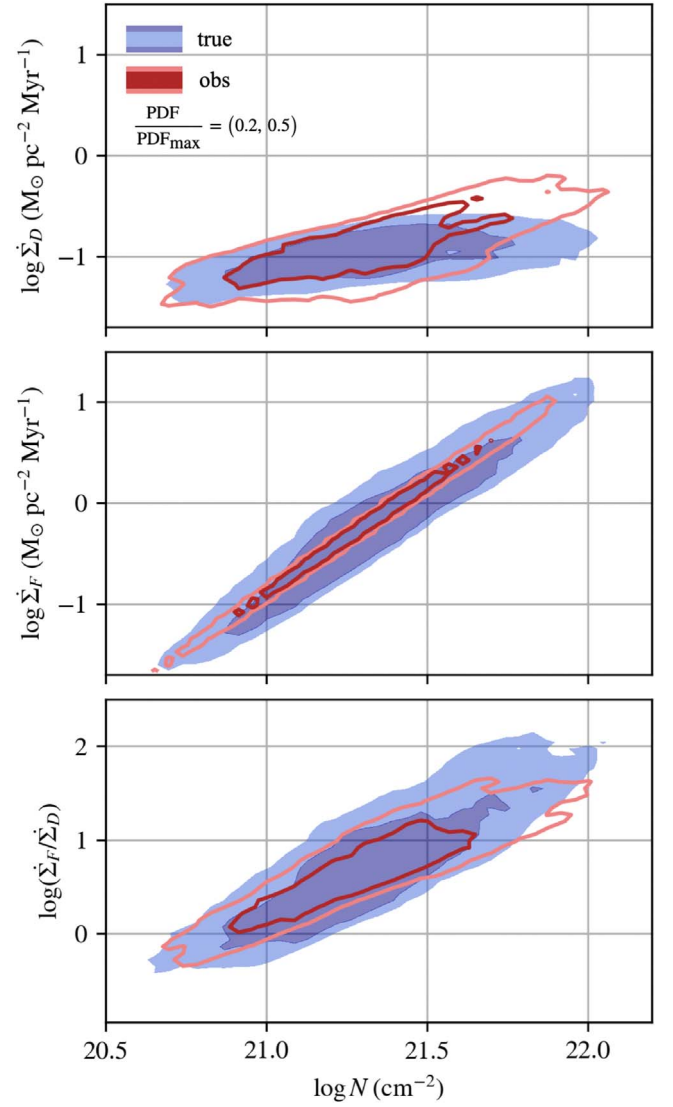

Figure 8. Mass-weighted mutual 2D PDFs of $\log N$, the total gas column density along the LOS, vs. $\log \dot{\Sigma}_D$ (top), $\log \dot{\Sigma}_F$ (middle), and $\log(\dot{\Sigma}_F/\dot{\Sigma}_D)$ (bottom). The red and blue PDFs correspond to the observationally-derived-rate (Equations (9) and (12)) and the true-rate (Equation (7)) PDFs, respectively. The light and dark red contours correspond to PDF/PDF$_{\max} = 0.2$ and 0.5, respectively. Similarly, the light blue shows the level $0.2 \leqslant$ PDF/PDF$_{\max} < 0.5$ and the darker blue shows the PDF region of PDF/PDF$_{\max} \geqslant 0.5$.

Comparing the PDFs in the top versus the middle panels, we see that the formation-rate PDFs have significantly larger dispersion compared to the dissociation-rate PDFs. This high dispersion in $\dot{\Sigma}_F$ is driven by the strong density fluctuations of the cloud, and the fact that for a significant fraction of the cloud mass the gas has not yet reached CSS (see Section 4.1).

This is further demonstrated in Figure 8, in which we show the joint (2D) mass-weighted PDFs of $\dot{\Sigma}_F$, $\dot{\Sigma}_D$, and $\dot{\Sigma}_F/\dot{\Sigma}_D$ versus the gas column density N. Both the formation and dissociation rates systematically increase with N. However, the formation rate has a steeper slope. Consequently, at large column densities, the H$_2$ formation rate surpasses the photodissociation rate. As discussed in Section 4.1, the cloud regions contributing to this excess formation are areas with high volume density, typically embedded deep in the cloud, which are in the process of converting H I into H$_2$ and have not yet reached CSS. If the MC were to maintain its physical

conditions for a sufficiently long time ($\gg t_{\rm chem}$), these regions would eventually convert most of their H I into H$_2$, reducing the formation rate until it balances with the dissociation rate. Such a balance has already been achieved (approximately) in the more diffuse cloud regions, at $N \lesssim 10^{21}$ cm^{-2}.

Figure 8 also highlights cloud regions where our method performs well statistically and where it is less accurate. For H$_2$ dissociation, in less dense cloud regions ($N \lesssim 2 \times 10^{21}$ cm^{-2}), the observationally derived rates closely match the true rates. In denser regions, however, the observationally derived rates generally overestimate the true rate. At $N = 3 \times 10^{21}$ cm^{-2}, this overestimation is typically a factor of 1.4 (comparing the means of the two PDFs), whereas at $N = 10^{22}$ cm^{-2}, the observational PDF's performance further declines, with the overestimation increasing to a factor of 2.2. As we discuss in Section 5.2, our method is not reliable at large columns in any

case, as CR dissociation may become significant in such environments. For H_2 formation, the observationally derived PDF statistically recovers the true PDF over the entire range of N. However, at any given N, it exhibits a systematically lower dispersion compared to the true-rate PDF.

These results demonstrate both the potential and limitations of our observational method for deriving H_2 formation and dissociation rates across various cloud conditions, setting the stage for a more detailed examination of its implications and applicability, which we discuss in the following section.

5. Discussion

As we show in this paper, large fractions of cloud masses may be far from CSS, with H_2 formation and dissociation not balancing each other. We demonstrate that observations of H_2 emission lines, in combination with gas column densities, may be used to constrain the H_2 formation and dissociation rates and to assess whether the gas along the observation LOS is in CSS. It is important to note that our method provides LOS-integrated rates. In real observations, multiple cloud structures may overlap along the same LOS. In such cases, our method can reveal if some portion of the gas is out of CSS, but it cannot resolve which specific clouds are responsible. This limitation suggests focusing initial applications on well-characterized single-cloud sightlines, such as high-latitude Galactic clouds.

5.1. Generalization to IR Line Emission

Since FUV line emission from H_2 excitation is followed by rovibrational cascades within the ground electronic state, it is accompanied by IR line emission (E. F. van Dishoeck & J. H. Black 1986; J. H. Black & E. F. van Dishoeck 1987; A. Sternberg 1988; A. Sternberg & A. Dalgarno 1989). This H_2 line emission has been observed in a variety of sources (e.g., I. Gatley et al. 1987; H. L. Dinerstein et al. 1988; P. J. Puxley et al. 1988; M. Tanaka et al. 1989, 1991; K. F. Kaplan et al. 2021). These IR emission lines can also be used to estimate the integrated H_2 photodissociation rate.

While IR line emission can be used to derive the H_2 photodissociation rate, a complication arises, because these transitions originate from rovibrationally excited H_2 states, which can be excited by various mechanisms beyond photo-excitation, including collisional excitation in warm-gas regions (e.g., shocks), secondary electrons produced by penetrating CRs or X-rays, and chemical pumping during H_2 formation (Figure 1 in S. Bialy 2020). Consequently, deducing the H_2 photodissociation rate ($\dot{\Sigma}_D$) requires disentangling these various excitation processes. In contrast, FUV lines solely originate from photo-excitation, providing a more direct relation to the H_2 photodissociation rate, although IR line emission has the advantage of being less affected by dust extinction, allowing the probing of deeper cloud regions. Ideally, both FUV and IR lines should be used in tandem to: (a) verify the consistency of the H_2 dissociation rate derived from both methods; (b) assess the impact of dust extinction on H_2 line emission; and (c) determine the roles of the various excitation mechanisms.

Assuming the subtraction of H_2 line emission due to alternative excitation processes, we may write a relation for the H_2 photodissociation rate in terms of the IR line emission. Following the derivation of Equation (A4) (see Appendix A),

we obtain

$$
\begin{aligned}
\dot{\Sigma}_D^{(\mathrm{obs})} &= \frac{4\pi p_{\mathrm{diss}} \bar{m}}{(1 - p_{\mathrm{diss}})} \frac{\mathcal{I}_{\mathrm{tot}}^{\mathrm{IR}}}{\mathcal{N}^{\mathrm{IR}}} \\
&= 4.4 \times 10^{-2} \, \mathcal{I}_5^{\mathrm{IR}} \, M_\odot \mathrm{pc}^{-2}\mathrm{Myr}^{-1},
\end{aligned}
\tag{14}
$$

where $\mathcal{I}_{\mathrm{tot}}^{\mathrm{IR}}$ is the IR total line intensity, and $\mathcal{I}_5 \equiv \mathcal{I}_{\mathrm{tot}}^{\mathrm{IR}}/(10^5$ photons cm^{-2} s^{-1} str^{-1}). In Equation (14), we do not include the dust attenuation β_{dust} factor (see Appendix A, Equations (A3) and (A5)), because for the IR wavelength dust absorption is typically negligible. For a dust absorption cross section of 4.5×10^{-23} cm^2 per hydrogen nucleus (for the 2–3 μm wavelength range; B. T. Draine 2011), the gas remains optically thin up to gas column densities $N \approx 2 \times 10^{22}$ cm^{-2}.

The factor $\mathcal{N}^{\mathrm{IR}} = \mathcal{I}_{\mathrm{tot}}^{\mathrm{IR}}/\mathcal{I}_{\mathrm{tot}}$ is the ratio of IR to FUV photons emitted per H_2 photo-excitation. This factor arises because IR emission involves cascades through multiple rovibrational states, unlike FUV emission, where each excitation produces a single photon. For instance, when the excited H_2 state $B^1\Sigma_u^+$ decays to $X^1\Sigma_g^+$, it emits one FUV photon and leaves H_2 rovibrationally excited, which may then emit multiple IR photons (e.g., three photons in the path $v = 3 \to 2 \to 1 \to 0$). Using the Meudon PDR code data (F. Le Petit et al. 2006), we calculated $\mathcal{N}^{\mathrm{IR}}$ for various gas temperatures, considering photo-pumping from $X^1\Sigma_g^+$ to excited levels within $B^1\Sigma_u^+$ and $C^1\Pi^u$, assuming a Boltzmann distribution for $X^1\Sigma_g^+$ rovibrational states and a B. T. Draine (1978) FUV radiation spectrum. Using Einstein A coefficients, we computed the decay probabilities and the resulting FUV and IR line emissions. For $T = 100$ K, we found $\mathcal{N}^{\mathrm{IR}} = 3.6$, a value that varies little (standard deviation 0.09 and min–max variation 0.3) for temperatures between 10 and 1000 K, indicating that $\mathcal{N}^{\mathrm{IR}}$ remains relatively constant across a wide range of temperatures relevant to MCs.

In terms of the photon number, the total IR line emission is higher, while the energy surface brightness (erg cm^{-2} s^{-1} sr^{-1}) is greater in the FUV, due to the higher energies carried by the FUV photons.

5.2. Additional H₂ Destruction Processes

Our model focuses on H_2 photodissociation, neglecting other destruction mechanisms such as CR ionization and dissociation, X-ray ionization, and collisional dissociation in warm/hot gas. It is thus best suited for standard MCs that are typically cold ($\ll 10^4$ K) and not exposed to abnormally strong X-ray or CR fluxes. In Appendix B, we describe a detailed model explicitly calculating the effect of CR ionization on the H_2 removal rate compared to FUV photodissociation. For a typical CR ionization rate of $\zeta_0 = 10^{-16}$ s^{-1}, CR destruction remains negligible compared to photodissociation for LOSs with column densities $N \lesssim 2 \times 10^{22}$ cm^{-2} (see Appendix B and Figure 9), consistent with analytic model predictions (A. Sternberg et al. 2024). X-rays similarly affect H_2 destruction, producing secondary electrons that lead to H_2 ionization and dissociation analogous to CRs.

In regions with abnormally high CR or X-ray fluxes, an apparent imbalance between H_2 formation and dissociation rates (as measured by FUV emission lines) may be observed, even if H_2 is in CSS, because FUV emission lines only reflect the contribution from FUV excitation and photodissociation, not the total H_2 removal rate (although at sufficiently high

fluxes or column densities, CRs may also contribute to FUV line emission; M. Padovani et al. 2024). For such clouds, the additional contribution of CR ionization and dissociation to H_2 removal can be constrained by observing various molecular ions (e.g., H_3^+, OH^+, H_2O^+, and ArH^+) in absorption spectroscopy (e.g., F. F. S. van der Tak & E. F. van Dishoeck 2000; N. Indriolo & B. J. McCall 2012; D. A. Neufeld & M. G. Wolfire 2017; S. Bialy et al. 2019). Alternatively, the CR contribution may be derived from H_2 observations by targeting specific IR emission lines (within the 2–3 μm range) produced by CR-excited H_2, with the relative contribution of CR-excited versus UV-excited H_2 lines constrained by line ratios (S. Bialy 2020; B. A. L. Gaches et al. 2022; M. Padovani et al. 2022). These lines may be observable with the NIRSpec spectrograph on JWST or, for exceptionally bright CR fluxes, by ground-based observatories (S. Bialy et al. 2022, 2024).

5.3. Observations of H_2 in the FUV and IR

The H_2 IR emission lines can be observed with JWST's complementary instruments: NIRSpec and MIRI. NIRSpec (P. Jakobsen et al. 2022) offers low-resolution ($R = 100$) prism spectroscopy over the entire wavelength range $\lambda = 0.6$–5.3 μm, as well as medium-to-high-resolution ($R = 1000$–2700) gratings covering various wavelength intervals within this range. The MIRI instrument (P. Bouchet et al. 2015) extends the observable H_2 IR line emission spectrum to longer wavelengths.

No FUV instrument has had or currently has the ability to resolve the H_2 fluorescent lines over the large solid angles spanned by MCs. FUV H_2 emission from individual protoplanetary disks was measured by the Hubble Space Telescope Cosmic Origins Spectrograph (G. J. Herczeg et al. 2004, 2006) and rocket-borne experiments (K. Hoadley et al. 2014, 2016). Low-spatial- and low-spectral-resolution measurements spanning 70% of the sky with the FIMS/SPEAR mission (Y.-S. Jo et al. 2017) showed intense H_2 emission from star-forming regions across our Galaxy. However, the spectral resolution of less than 1000 was too low to separate individual fluorescent lines and determine the excitation conditions, while the spatial resolution of about 5′ was coarser than the clouds' scales of variation, leading to great uncertainty in characterizing the H_2 formation and dissociation rates in even the nearest clouds.

The lack of FUV observations of H_2 has inspired several mission concepts. Building on a well-received but not selected initial proposal for a Medium Explorer–class space telescope (E. T. Hamden et al. 2022), we have refined the concept to match NASA's Small Explorer opportunity. This revised mission, named Eos, is designed to measure FUV lines from nearby star-forming regions with spectral resolution $R > 10,000$, sufficient to distinguish individual fluorescent lines. Eos will achieve an angular resolution of $<10''$ over a spectrograph slit several degrees long, enabling a detailed resolution of cloud structures while providing coverage adequate for assessing global evolutionary states. The Eos telescope will implement the measurement approach outlined in this paper, covering thousands of square degrees on the sky during a 2 yr primary mission and surveying nearly all nearby MCs. A brief description of some of the mission objectives can be found in E. T. Hamden et al. (2024). Eos will, for the first time, determine the extent of MCs out of CSS and address fundamental questions about cloud origins, evolution, and dispersal in their role as stellar nurseries. Eos will be proposed in 2025 to the expected NASA Small Explorer announcement of opportunity, with a launch date in the early 2030s.

6. Conclusions

In this study, we have investigated the photodissociation and formation processes of H_2 in simulated MCs, with a particular focus on utilizing FUV and IR line emissions to constrain these rates. Our key findings are as follows:

1. A significant fraction of MC mass and volume is out of CSS, due to rapid dynamical evolution, with H_2 formation rates either exceeding or lagging behind photodissociation rates (Tables 1–2).
2. The total intensity of the H_2 line emission, whether measured in the FUV or IR, can effectively constrain the LOS-integrated H_2 photodissociation rate $\dot{\Sigma}_D$ (Equations (9) and (14)).
3. Measurements of H I and the total gas column density provide a means to constrain the integrated H_2 formation rate, $\dot{\Sigma}_F$ (Equation (12)).
4. By combining H_2 line emission and gas column densities, we can determine the chemical state of gas along the LOS: CSS ($\dot{\Sigma}_F/\dot{\Sigma}_D \approx 1$), active H_2 formation ($\dot{\Sigma}_F/\dot{\Sigma}_D \gg 1$), or active photodissociation ($\dot{\Sigma}_F/\dot{\Sigma}_D \ll 1$) (Equation (13)).
5. CSS assessment reveals key aspects of MC evolution. MCs far from CSS suggest recent rapid changes—either fresh gas inflow or quick evaporation. These changes happen faster than the time needed for chemical balance (Equation (5)).

These findings provide valuable insights into the dynamics of H_2 in MCs and offer observational strategies for probing the chemical and physical states of these complex systems. Our results underscore the importance of considering non-steady-state conditions in MC studies and highlight the potential of using molecular line emissions as diagnostic tools for cloud evolution.

Appendix A
The $\dot{\Sigma}_D - \mathcal{I}_{\text{tot}}$ Relation

We derive the relationship between the integrated H_2 photodissociation rate, $\dot{\Sigma}_D$, and the total H_2 line emission intensity, $\mathcal{I}_{\text{tot}}$. Following S89, the total photon intensity for a uniform-density 1D slab is given by

$$\mathcal{I}_{\text{tot}} = \frac{1}{4\pi}(1 - p_{\text{diss}}) \int_0^L n(H_2)\chi P_0 e^{-2\tau} f_{H_2,\text{shield}}\, ds \quad (A1)$$

$$= \frac{1}{4\pi}(1 - p_{\text{diss}}) \int_0^L n(H_2)P e^{-\tau}\, ds. \quad (A2)$$

To derive this relation, we start with Equation (A1) in S89, which describes the intensity of a single H_2 emission line. We sum over the branching ratios (denoted as b in S89) for transitions to bound rovibrational states, introducing the factor $(1 - p_{\text{diss}})$ in our Equations (A1)–(A2). In these equations, P_0 is the unattenuated photo-excitation rate for a unit Draine (B. T. Draine 1978) radiation field, while P is the local attenuated H_2 photo-excitation rate at cloud depth s. For slab geometry, $P = \chi P_0 f_{H_2,\text{shield}}\, e^{-\tau}$, where $f_{H_2,\text{shield}}$ is the H_2 self-shielding function (e.g., B. T. Draine & F. Bertoldi 1996) and $\tau = \int_0^s \sigma n\, ds'$ is the dust opacity from point s to the cloud's edge, with $\sigma = 1.9 \times 10^{-21}$ cm^2 being the dust absorption cross section per hydrogen nucleus averaged over the LW band.

Our notation differs from S89: our P_0 and D_0 correspond to their P and D, and they denote H_2 self-shielding as $f(N_2)$. In Equations (A1)–(A2), we integrate emission through the cloud (from $s = 0$ to $s = L$) along the LOS. The factor of 2 in the exponent of Equation (A1) accounts for dust absorption in both directions: first, as LW radiation propagates from the cloud edge inward, exciting H_2; and second, as the resulting emission lines travel outward. Unlike FUV continuum radiation, which experiences both dust absorption and H_2 self-shielding, H_2 emission lines are primarily attenuated by dust alone. This is because most H_2 in the cloud occupies low rovibrational states and thus does not re-absorb these emission lines that mostly correspond to high rovibrational lower states. However, this approach is an approximation, as some self-absorption can occur and may alter the H_2 emission spectrum at shorter wavelengths (J. Le Bourlot 2024, private communication).

Examining Equation (A2), we notice its similarity to $\dot{\Sigma}_D^{\text{(true)}}$ (Equation (7)), differing only by a constant multiplication term and an exponential term in the integral. To express $\mathcal{I}_{\text{tot}}$ in terms of $\dot{\Sigma}_D^{\text{(true)}}$, we first define an effective attenuation factor:

$$\beta_{\text{dust}} \equiv \frac{\int n(H_2) D e^{-\tau}\, ds}{\int n(H_2) D\, ds}. \quad (A3)$$

Using this definition, we can combine Equation (A2) with Equation (7) to derive a relation between the H_2 line intensity and the integrated H_2 photodissociation rate:

$$\mathcal{I}_{\text{tot}} = \frac{1 - p_{\text{diss}}}{4\pi p_{\text{diss}}\bar{m}} \beta_{\text{dust}} \dot{\Sigma}_D^{\text{(true)}}. \quad (A4)$$

In this derivation, we utilize the relationship $P = D/p_{\text{diss}}$ (Equation (8)).

The β_{dust} factor accounts for the reduction in line emission due to dust absorption as photons propagate from the cloud interior to the observer. However, direct measurement of β_{dust} is challenging, as it depends on the 3D density structure along the LOS and the radiation geometry. While 3D dust maps provide information on density structure (e.g., R. Leike et al. 2020), they typically cannot resolve the critical H I–H$_2$ transition length, which usually occurs over scales $\lesssim 1$ pc (S. Bialy et al. 2017). In the absence of 3D information, we approximate β_{dust} using the simplest possible geometry: a 1D uniform slab where H_2 line emission and dust absorption occur, with total dust optical depth $\tau_{\text{tot}} = \int_0^L \sigma n\, ds = \sigma N$, where N is the integrated gas column density along the entire LOS. Assuming equal line emission per unit dust optical depth $d\tau$, we can express β_{dust} as

$$\beta_{\text{dust}}^{\text{(obs)}} = \int_0^{\tau_{\text{tot}}} \left(\frac{d\tau}{\tau_{\text{tot}}}\right) e^{-\tau}$$

$$= \frac{1 - e^{-\tau_{\text{tot}}}}{\tau_{\text{tot}}} = \frac{1 - e^{-1.9N_{21}}}{1.9N_{21}}. \quad (A5)$$

This expression is the exact solution given by the equation of transfer for attenuation in a medium where emitters are fully mixed with absorbers, and it is analogous to the escape probability formalism. In the last equality, we use $\sigma = 1.9 \times 10^{-21}$ cm^{-2} and define $N_{21} \equiv N/(10^{21}\ \text{cm}^{-2})$, yielding $\tau_{\text{tot}} = 1.9N_{21}$. In the limit $\tau_{\text{tot}} \ll 1$, $\beta_{\text{dust,obs}} \to 1$, approaching the optically thin limit. Conversely, when $\tau_{\text{tot}} \gg 1$, $\beta_{\text{dust,obs}} \to 1/\tau_{\text{tot}}$. This is because in the optically thick limit, the LOS contains $\sim \tau_{\text{tot}}$ transition layers (each with opacity ~ 1), but we receive signals only from emission lines to a depth of $\tau_{\text{tot}} \sim 1$, resulting in relative emission $\propto 1/\tau_{\text{tot}}$.

Substituting Equation (A5) for β_{dust} in Equation (A4), we obtain

$$\dot{\Sigma}_D^{\text{(obs)}} = \frac{4\pi p_{\text{diss}}\bar{m}}{1 - p_{\text{diss}}}\ \mathcal{I}_{\text{tot}}\ \left(\frac{\tau_{\text{tot}}}{1 - e^{-\tau_{\text{tot}}}}\right)$$

$$= 0.3\ \mathcal{I}_5 \left(\frac{N_{21}}{1 - e^{-1.9N_{21}}}\right) M_\odot \text{pc}^{-2}\text{Myr}^{-1}, \quad (A6)$$

where in the numerical evaluation we use $\tau_{\text{tot}} = 1.9N_{21}$ and define $\mathcal{I}_5 \equiv \mathcal{I}_{\text{tot}}/(10^5$ photons cm^{-2} s^{-1} sr^{-1}). The superscript "(obs)" in Equations (A5) and (A6) emphasizes that these expressions provide approximations to the true attenuation factor and H_2 photodissociation rates, as they rely on observable (integrated) quantities.

Appendix B
H$_2$ Destruction by CRs

To assess the contribution of CRs to H_2 removal, we calculate the individual contributions of FUV and CRs to H_2 dissociation on a cell-by-cell basis in our simulation. In each cell, the H_2 removal rate (in s^{-1}) by CRs is

$$D_{\text{CR}} = \varphi \zeta, \quad (B1)$$

where ζ (s^{-1}) is the total H_2 ionization rate by primary CRs and secondary electrons, and φ is the number of H_2 molecules destroyed per ionization event. This includes H_2 ionization by CRs, H_2 dissociation via chemical reactions with CR-produced ions, and direct H_2 dissociation by CRs. Following A. Sternberg et al. (2024), we adopt $\varphi = 2$. The CR ionization rate is
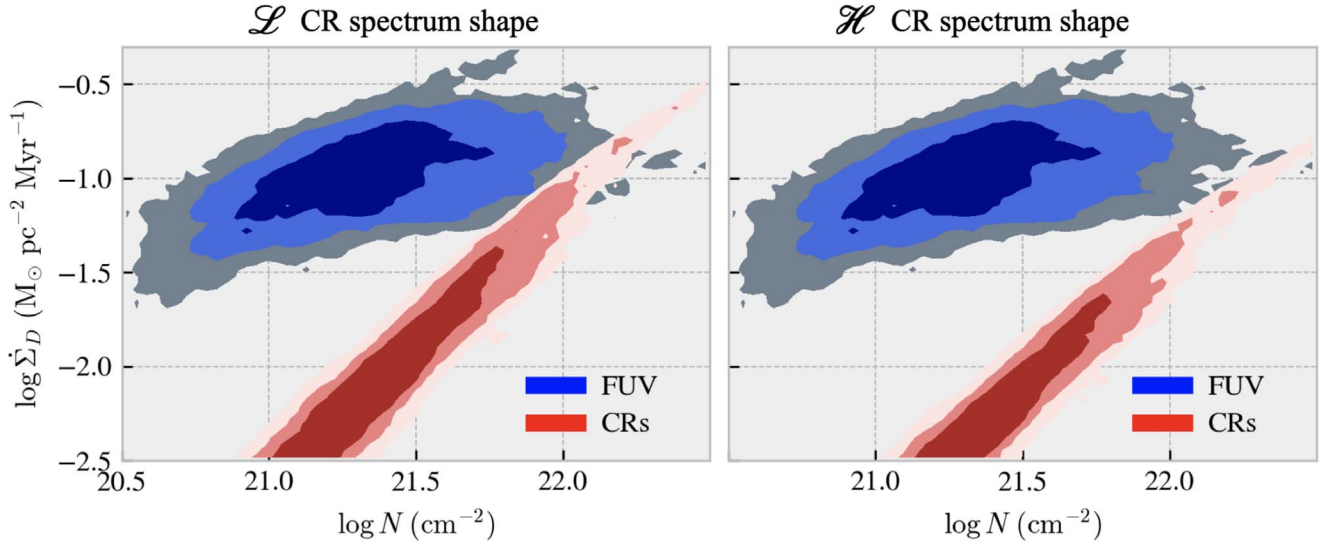
Figure 9. Contributions of FUV radiation and CRs to H_2 removal as a function of LOS column density. The left panel shows results for the $\mathcal{L}$ CR-spectral-shape model, while the right panel represents the $\mathcal{H}$ model (these models are discussed in M. Padovani et al. 2018). Both assume an unattenuated CR ionization rate of $\zeta_0 = 10^{-16} \, s^{-1}$ and $N_0 = 10^{19} \, cm^{-2}$ (see Equations (B1)–(B2)). The shaded regions represent contours of the 2D PDF of $\log \dot{\Sigma}_D$ vs. $\log N$, with light to dark shades corresponding to PDF/PDF$_{max}$ levels that fall within the ranges (0.03, 0.1), (0.1, 0.3), and (0.3, 1), respectively. The figure demonstrates that for column densities $N \lesssim 2 \times 10^{22} \, cm^{-2}$, FUV photodissociation dominates over CR-induced H_2 removal, consistent with A. Sternberg et al. (2024).

given by

$$\zeta = \begin{cases} \zeta_0 & \text{if } N_{eff} < N_0 \\ \zeta_0 \left(\frac{N_{eff}}{N_0} \right)^{-\gamma} & \text{if } N_{eff} \geqslant N_0 \end{cases} \quad \text{(B2)}$$

This form accounts for CR attenuation as they propagate through the cloud, where N_{eff} represents an effective mean column density for CRs propagating in different directions, and ζ_0, N_0, and γ are constants. We approximate N_{eff} using the effective visual extinction $A_{V,eff}$, as calculated by the SILCC simulation, with $N_{eff} = 1.8 \times 10^{21} A_{V,eff} \, cm^{-2}$ (see B. A. L. Gaches et al. 2022 for a discussion of this approach). We consider the two CR energy-spectral-shape models $\mathcal{H}$ and $\mathcal{L}$ discussed by M. Padovani et al. (2018), for which $\gamma = 0.39$ and 0.28, respectively, and adopt the standard values $N_0 = 10^{19} \, cm^{-2}$ and $\zeta_0 = 10^{-16} \, s^{-1}$ (A. Sternberg et al. 2024). Using these equations, we calculate the H_2 removal rate by CRs on a cell-by-cell basis. We then integrate these rates along the LOS (Equation (7)) to obtain the CR contribution to the H_2 integrated removal rate, $\dot{\Sigma}_D$.

In Figure 9, we present the FUV and CR contributions to $\dot{\Sigma}_D$ as a function of the column density along the LOS, N. The left and right panels correspond to the $\mathcal{L}$ and $\mathcal{H}$ CR-spectral-shape models, respectively. The three shaded regions in each panel represent contours of the 2D PDF of $\log \dot{\Sigma}_D$ versus $\log N$. These contours correspond to PDF/PDF$_{max}$ levels in the ranges (0.03, 0.1), (0.1, 0.3), and (0.3, 1), depicted by light to dark shades, respectively. Our analysis shows that for LOSs with column densities $N \lesssim 2 \times 10^{22} \, cm^{-2}$, the CR contribution to H_2 removal is negligible compared to FUV photodissociation. This finding is consistent with the analytic model predictions of A. Sternberg et al. (2024). It is important to note that our chosen value of $\zeta_0 = 10^{-16} \, s^{-1}$ represents a standard CR ionization rate in the ambient ISM. However, in the vicinity of CR sources, such as supernova remnants, the CR flux may be significantly higher, resulting in an increased value of ζ_0. In such cases, the CR distribution shown in our figure would be

shifted upward in proportion to the increase in ζ_0. Consequently, the transition point where CR-induced H_2 removal becomes comparable to FUV photodissociation would occur at lower column densities.

Appendix C
Statistical Analysis of Multiple Snapshots

To validate the robustness of our methodology across different cloud conditions, we have analyzed multiple snapshots of our simulation. Specifically, we examined snapshots at $t = 2$, 4, and 5 Myr, in addition to our original snapshot at $t = 3$ Myr. For each time, we analyzed maps along three orthogonal LOSs, x, y, and z, resulting in a total of 12 realizations.

For each realization, we calculated the integrated dissociation and formation mass rates ($\dot{M}_D$ and $\dot{M}_F$) by integrating their corresponding surface density rates ($\dot{\Sigma}_D$ and $\dot{\Sigma}_F$) over the area. Specifically, integrating the observationally derived surface densities $\dot{\Sigma}_D^{(obs)}$ and $\dot{\Sigma}_F^{(obs)}$ using Equations (9) and (12) yields the observationally derived mass rates $\dot{M}_D^{(obs)}$ and $\dot{M}_F^{(obs)}$, while integrating the true surface densities $\dot{\Sigma}_D^{(true)}$ and $\dot{\Sigma}_F^{(true)}$ using Equation (7) yields the true mass rates $\dot{M}_D^{(true)}$ and $\dot{M}_F^{(true)}$. The true rates can also be calculated (identically) by volumetrically integrating the H_2 formation and dissociation volume rates j_F and j_D (Equation (2)) over the simulation volume. Since the true mass rates represent cloud-integrated quantities over the full volume, they are independent of orientation (x, y, or z), while the observationally derived rates depend on the viewing angle as they are estimated from 2D projected maps. We report these values in Table 2 and compare them via the absolute relative difference:

$$\Delta_D = \frac{|\dot{M}_D^{(obs)} - \dot{M}_D^{(true)}|}{\dot{M}_D^{(true)}}$$

$$\Delta_F = \frac{|\dot{M}_F^{(obs)} - \dot{M}_F^{(true)}|}{\dot{M}_F^{(true)}} . \quad \text{(C1)}$$
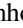
Table 2
H$_2$ Formation and Dissociation Rates for Multiple Snapshots

Time (Myr)	$\dot{M}_F^{\text{(true)}}$ $(10^3 M_\odot\ \text{Myr}^{-1})$	$\dot{M}_F^{\text{(obs)}}$	Δ_F	$\dot{M}_D^{\text{(true)}}$ $(10^3 M_\odot\ \text{Myr}^{-1})$	$\dot{M}_D^{\text{(obs)}}$	Δ_D
2	7.46	13.3	0.78	0.965	1.23	0.28
		8.90	0.19		1.42	0.48
		7.80	0.05		1.30	0.34
3 (Fiducial)	8.61	9.30	0.08	1.14	1.41	0.24
		10.8	0.26		1.47	0.29
		7.26	0.16		1.07	0.06
4	10.1	15.5	0.54	1.03	1.33	0.30
		9.15	0.09		1.47	0.43
		7.07	0.30		1.31	0.28
5	8.56	14.2	0.66	1.04	1.38	0.32
		8.47	0.01		1.49	0.43
		7.52	0.12		1.32	0.27

Note. For each snapshot time, we show the true rates from the simulation ($\dot{M}^{\text{(true)}}$) and observationally derived rates ($\dot{M}^{\text{(obs)}}$) for H$_2$ formation and dissociation. Each snapshot contains three rows corresponding to orthogonal viewing angles (x, y, and z LOS orientations). The relative differences Δ are calculated using Equation (C1). Our fiducial snapshot ($t = 3$ Myr) that is analyzed throughout the paper is highlighted in boldface. The statistics shown at the bottom are computed across all measurements (12 realizations: four snapshots × three LOS orientations).

Across all 12 realizations, we find mean relative differences of $\bar{\Delta}_D = 0.31$ and $\bar{\Delta}_F = 0.27$, with median values of 0.29 and 0.18 for dissociation and formation, respectively (see Table 2 for more details).

ORCID iDs

Shmuel Bialy ⓘ https://orcid.org/0000-0002-0404-003X
Blakesley Burkhart ⓘ https://orcid.org/0000-0001-5817-5944
Daniel Seifried ⓘ https://orcid.org/0000-0002-0368-9160
Mark R. Krumholz ⓘ https://orcid.org/0000-0003-3893-854X
Stefanie Walch ⓘ https://orcid.org/0000-0001-6941-7638
Erika Hamden ⓘ https://orcid.org/0000-0002-3131-7372
Thomas J. Haworth ⓘ https://orcid.org/0000-0002-9593-7618
Neal J. Turner ⓘ https://orcid.org/0000-0001-8292-1943
Min-Young Lee ⓘ https://orcid.org/0000-0002-9888-0784
Shuo Kong ⓘ https://orcid.org/0000-0002-8469-2029

References

Abgrall, H., Le Bourlot, J., Pineau Des Forets, G., et al. 1992, A&A, 253, 525
Barkana, R., & Loeb, A. 2001, PhR, 349, 125
Bialy, S. 2020, CmPhy, 3, 32
Bialy, S., Belli, S., & Padovani, M. 2022, A&A, 658, L13
Bialy, S., Burkhart, B., & Sternberg, A. 2017, ApJ, 843, 92
Bialy, S., Neufeld, D., Wolfire, M., Sternberg, A., & Burkhart, B. 2019, ApJ, 885, 109
Bialy, S., & Sternberg, A. 2015, MNRAS, 450, 4424
Bialy, S., & Sternberg, A. 2016, ApJ, 822, 83
Bialy, S., & Sternberg, A. 2019, ApJ, 881, 160
Bialy, S., Sternberg, A., Lee, M.-Y., Petit, F. L., & Roueff, E. 2015, ApJ, 809, 122
Bialy, S., Zucker, C., Goodman, A., et al. 2021, ApJL, 919, L5
Bialy, S., Belli, S., Bisbas, T. G., et al. 2024, Constraining Cosmic Rays with H2 Ro-Vibrational Excitation in Dense Clouds, JWST Proposal. Cycle 3, ID. #5064
Bigiel, F., Leroy, A., Walter, F., et al. 2008, AJ, 136, 2846
Bisbas, T. G., Schruba, A., & Van Dishoeck, E. F. 2019, MNRAS, 485, 3112
Bisbas, T. G., Tan, J. C., & Tanaka, K. E. I. 2021, MNRAS, 502, 2701
Black, J. H., & van Dishoeck, E. F. 1987, ApJ, 322, 412
Bolatto, A. D., Wolfire, M., & Leroy, A. K. 2013, ARA&A, 51, 207
Bouchet, P., García-Marín, M., Lagage, P.-O., et al. 2015, PASP, 127, 612
Bromm, V., Ferrara, A., Coppi, P., & Larson, R. 2001, MNRAS, 328, 969
Burkhart, B., Bialy, S., Seifried, D., et al. 2024, ApJ, 975, 269
Chevance, M., Krumholz, M. R., McLeod, A. F., et al. 2023, in ASP Conf. Ser. 534, Protostars and Planets VII, ed. S. Inutsuka et al. (San Francisco, CA: ASP), 1
Dalgarno, A. 2006, PNAS, 103, 12269
Dalgarno, A., Herzberg, G., & Stephens, T. L. 1970, ApJL, 162, L49
Dawson, J. R. 2013, PASA, 30, e025
Dinerstein, H. L., Lester, D. F., Carr, J. S., & Harvey, P. M. 1988, ApJL, 327, L27
Draine, B. T. 1978, ApJS, 36, 595
Draine, B. T. 2011, Physics of the Interstellar and Intergalactic Medium (Princeton, NJ: Princeton Univ. Press)
Draine, B. T., & Bertoldi, F. 1996, ApJ, 468, 269
Faucher-Giguère, C. A., Quataert, E., & Hopkins, P. F. 2013, MNRAS, 433, 1970
Field, G. B., Somerville, W. B., & Dressler, K. 1966, ARA&A, 4, 207
Gaches, B. A. L., Bisbas, T. G., & Bialy, S. 2022, A&A, 658, A151
Galli, D., & Palla, F. 1998, A&A, 335, 403
Gatley, I., Hasegawa, T., Hiroko, S., et al. 1987, ApJL, 318, L73
Girichidis, P., Walch, S., Naab, T., et al. 2016, MNRAS, 456, 3432
Glover, S. C. O., & Mac Low, M.-M. 2007, ApJ, 659, 1317
Goldshmidt, O., & Sternberg, A. 1995, ApJ, 439, 256
Goldsmith, P. F., Li, D., & Krčo, M. 2007, ApJ, 654, 273
Haiman, Z., Rees, M. J., & Loeb, A. 1996, ApJ, 467, 522
Hamden, E. T., Schiminovich, D., Nikzad, S., et al. 2022, JATIS, 8, 044008
Hamden, E. T., Schiminovich, D., Turner, N. J., et al. 2024, Proc. SPIE, 13093, 130930C
Harris, C. R., Millman, K. J., van der Walt, S. J., et al. 2020, Natur, 585, 357
Hartmann, L., Ballesteros-Paredes, J., & Bergin, E. A. 2002, ApJ, 562, 852
Herbst, E., & Klemperer, W. 1973, ApJ, 185, 505
Herczeg, G. J., Linsky, J. L., Walter, F. M., Gahm, G. F., & Johns-Krull, C. M. 2006, ApJS, 165, 256
Herczeg, G. J., Wood, B. E., Linsky, J. L., Valenti, J. A., & Johns-Krull, C. M. 2004, ApJ, 607, 369
Hoadley, K., France, K., Nell, N., et al. 2014, Proc. SPIE, 9144, 914406
Hoadley, K., France, K., Kruczek, N., et al. 2016, Proc. SPIE, 9905, 99052V
Hollenbach, D., & McKee, C. F. 1979, ApJS, 41, 555
Hollenbach, D. J., & Tielens, A. G. G. M. 1999, RvMP, 71, 173
Hopkins, P. F., Chan, T. K., Garrison-Kimmel, S., et al. 2020, MNRAS, 3498, 3465
Hu, C.-Y., Naab, T., Walch, S., Glover, S. C. O., & Clark, P. C. 2016, MNRAS, 458, 3528
Hu, C.-Y., Sternberg, A., & van Dishoeck, E. F. 2021, ApJ, 920, 44
Hunter, J. D. 2007, CSE, 9, 90
Indriolo, N., & McCall, B. J. 2012, ApJ, 745, 91
Jakobsen, P., Ferruit, P., Alves de Oliveira, C., et al. 2022, A&A, 661, A80
Jeffreson, S. M. R., Semenov, V. A., & Krumholz, M. R. 2024, MNRAS, 527, 7093
Jo, Y.-S., Seon, K.-I., Min, K.-W., Edelstein, J., & Han, W. 2017, ApJS, 231, 21
Kaplan, K. F., Dinerstein, H. L., Kim, H., & Jaffe, D. T. 2021, ApJ, 919, 27
Koyama, H., & Inutsuka, S.-I. 2000, ApJ, 532, 980
Krumholz, M. R. 2012, ApJ, 759, 9
Krumholz, M. R., McKee, C. F., & Tumlinson, J. 2008, ApJ, 689, 865
Krumholz, M. R., McKee, C. F., & Tumlinson, J. 2009, ApJ, 693, 216
Le, H. A. N., Pak, S., Kaplan, K., et al. 2017, ApJ, 841, 13
Le Petit, F., Nehme, C., Le Bourlot, J., & Roueff, E. 2006, ApJS, 164, 506
Leike, R., Glatzle, M., & Enßlin, T. A. 2020, A&A, 639, A138
Leroy, A. K., Walter, F., Brinks, E., et al. 2008, AJ, 136, 2782
Luhman, M. L., Jaffe, D. T., Keller, L. D., & Pak, S. 1994, ApJL, 436, L185
Maloney, P. R., Hollenbach, D. J., & Tielens, A. G. G. M. 1996, ApJ, 466, 561
McKee, C. F., & Ostriker, E. C. 2007, ARA&A, 45, 565
McKee, C. F., & Ostriker, J. P. 1977, ApJ, 218, 148
Neufeld, D. A., & Spaans, M. 1996, ApJ, 473, 894
Neufeld, D. A., & Wolfire, M. G. 2017, ApJ, 845, 163
Noterdaeme, P., Balashev, S., Krogager, J. K., et al. 2019, A&A, 627, A32
Ntormousi, E., Burkert, A., Fierlinger, K., & Heitsch, F. 2011, ApJ, 731, 13
Omukai, K. 2000, ApJ, 534, 809
Orr, M. E., Fielding, D. B., Hayward, C. C., & Burkhart, B. 2022, ApJL, 924, L28
Ostriker, E. C., & Kim, C.-G. 2022, ApJ, 936, 137
Padovani, M., Galli, D., Ivlev, A. V., Caselli, P., & Ferrara, A. 2018, A&A, 619, A144
Padovani, M., Galli, D., Scarlett, L. H., et al. 2024, A&A, 682, A131
Padovani, M., Bialy, S., Galli., D., et al. 2022, A&A, 658, A189
Planck Collaboration, et al. 2011, A&A, 536, A19

Pound, M. W., & Wolfire, M. G. 2023, AJ, 165, 25
Puxley, P. J., Hawarden, T. G., & Mountain, C. M. 1988, MNRAS, 234, 29P
Ranjan, A., Noterdaeme, P., Krogager, J.-K., et al. 2018, A&A, 618, A184
Richings, A. J., Schaye, J., & Oppenheimer, B. D. 2014, MNRAS, 442, 2780
Röllig, M., & Ossenkopf-Okada, V. 2022, A&A, 664, A67
Röllig, M., Abel, N. P., Bell, T., et al. 2007, A&A, 467, 187
Schruba, A., Bialy, S., & Sternberg, A. 2018, ApJ, 862, 110
Schruba, A., Leroy, A. K., Walter, F., et al. 2011, AJ, 142, 37
Seifried, D., Beuther, H., Walch, S., et al. 2022, MNRAS, 512, 4765
Seifried, D., Haid, S., Walch, S., Borchert, E. M. A., & Bisbas, T. G. 2020, MNRAS, 492, 1465
Seifried, D., Walch, S., Reissl, S., & Ibáñez-Mejía, J. C. 2019, MNRAS, 482, 2697
Seifried, D., Walch, S., Girichidis, P., et al. 2017, MNRAS, 472, 4797
Stecher, T. P., & Williams, D. A. 1967, ApJL, 149, L29
Sternberg, A. 1988, ApJ, 332, 400
Sternberg, A. 1989, ApJ, 347, 863
Sternberg, A., Bialy, S., & Gurman, A. 2024, ApJ, 960, 8
Sternberg, A., & Dalgarno, A. 1989, ApJ, 338, 197
Sternberg, A., Petit, F. L., Roueff, E., & Bourlot, J. L. 2014, ApJS, 790, 10S

Syed, J., Soler, J. D., Beuther, H., et al. 2022, A&A, 657, A1
Tacconi, L. J., Genzel, R., & Sternberg, A. 2020, ARA&A, 58, 157
Tanaka, M., Hasegawa, T., & Gatley, I. 1991, ApJ, 374, 516
Tanaka, M., Hasegawa, T., Hayashi, S. S., Brand, P. W. J. L., & Gatley, I. 1989, ApJ, 336, 207
Tielens, A. G. G. M. 2013, RvMP, 85, 1021
Tielens, A. G. G. M., & Hollenbach, D. 1985, ApJ, 291, 722
Valdivia, V., Hennebelle, P., Gérin, M., & Lesaffre, P. 2016, A&A, 587, A76
van der Tak, F. F. S., & van Dishoeck, E. F. 2000, A&A, 358L, 79V
van Dishoeck, E. F., & Black, J. H. 1986, ApJS, 62, 109
van Dishoeck, E. F., Herbst, E., & Neufeld, D. A. 2013, ChRv, 113, 9043
Virtanen, P., Gommers, R., Oliphant, T. E., et al. 2020, NatMe, 17, 261
Wakelam, V., Bron, E., Cazaux, S., et al. 2017, MolAs, 9, 1
Walch, S., Girichidis, P., Naab, T., et al. 2015, MNRAS, 454, 238
Wolfire, M. G., McKee, C. F., Hollenbach, D., & Tielens, A. G. G. M. 2003, ApJ, 587, 278
Wolfire, M. G., Vallini, L., & Chevance, M. 2022, ARA&A, 60, 247
Wünsch, R., Walch, S., Dinnbier, F., & Whitworth, A. 2018, MNRAS, 475, 3393
Zucker, C., Goodman, A., Alves, J., et al. 2021, ApJ, 919, 35